Student thesis series INES nr 610

Spatial downscaling of gridded soil moisture products using optical and thermal satellite data: the effects of using different vegetation indices

Tómas Halldórsson Alexander

2023
Department of
Physical Geography and Ecosystem Science
Lund University
Sölvegatan 12
S-223 62 Lund
Sweden

Tómas Halldórsson Alexander (2023).
Spatial downscaling of gridded soil moisture products using optical and thermal satellite data: the effects of using different vegetation indices
Master degree thesis, 30 credits in *Geomatics*
Department of Physical Geography and Ecosystem Science, Lund University

Level: Master of Science (MSc)

Course duration: *January* 2023 until *June* 2023

Disclaimer

Spatial downscaling of gridded soil moisture products using optical and thermal satellite data: the effects of using different vegetation indices

---

Tómas Halldórsson Alexander

Master thesis, 30 credits, in *Geomatics*

Supervisor:
Zheng Duan
Dep. of Physical Geography and Ecosystem Science, Lund University

Co-supervisors:
Hongxiao Jin
Haijun Luan
Dep. of Physical Geography and Ecosystem Science, Lund University

Exam committee:
Paul Miller
Zhanzhang Cai
Dep. of Physical Geography and Ecosystem Science, Lund University

Acknowledgements

Firstly, I would like to thank Zheng Duan, Hongxiao Jin and Haijun Luan for all their help and guidance throughout the process. I would also like to thank my examiner Paul Miller and opponent Anna Schultze for their valuable feedback and comments which helped me further refine and improve my research.

To my friends and family, I would like to give thanks for continued support, and especially to my friend Sigurlaug Birna Guðmundsdóttir, who has consistently supported and encouraged me by my side throughout my studies.

Lastly, I would like to thank all the researchers, coders and programmers who have contributed to this topic and have laid an important foundation for my research.

Abstract

Soil moisture (SM) plays an important role in the exchange of heat and water between the surface and atmosphere, impacting water and energy cycles and the climate. Satellite remote sensing offers a global-scale estimation of SM; however, the coarse resolutions of satellite SM products, typically ranging from 25-50 km, are unsuitable for regional analysis. To overcome this limitation, various spatial downscaling methods have been developed to disaggregate SM products at coarse resolution to estimates at higher resolution. One commonly used approach is the optical and thermal-based method, which utilizes higher resolution ancillary data, such as land surface temperatures (LST) and vegetation indices (VI), within a triangular feature space. Previous studies have primarily relied on the use of NDVI (Normalised difference Vegetation Index) or EVI (Enhanced Vegetation Index) as VIs, neglecting the potential benefits of newly proposed VIs for spatial downscaling. Consequently, few studies have investigated the influence of different VIs on the downscaling of gridded soil moisture. This study aims to investigate the influences of using different VIs on spatial downscaling of the coarse resolution SM product. Two study areas are focused on in this study (1) an area around the SMOSMANIA network in southern France with 18 SM measurement stations and (2) an area surrounding the REMEDHUS network in northern Spain with 17 measurement stations. The daily ESA CCI SM product at 0.25° resolution was spatially downscaled using four different VIs including the NDVI, EVI, the kernel NDVI (kNDVI) and Plant Phenology Index (PPI) to produce a higher resolution SM product at 1 km and 16-day resolutions. All four VIs and the LST were obtained from MODIS products. The Vegetation Temperature Condition Index (VTCI) based downscaling approach was used for this study, in which wet and dry edges of the triangular feature space were determined by fitting a linear line to the maximum and minimum temperatures, respectively, for each VI interval. Evaluation showed that using PPI showed better consistency between two study areas, having the good correlation and ubRMSD against the in-situ measurements, whilst the performance of using other VIs particularly EVI and kNDVI varied in the study area. Using NDVI generally yielded the poorest overall performance in terms of ubRMSD and correlation, but it outperformed kNDVI in areas with generally sparser vegetation within the SMOSMANIA network. Comparison of SM product at the original coarse resolution and spatially downscaled SM, the ESA CCI SM product generally outperformed the downscaled SM products, with only 12 out of 35 stations showing superior performance for the downscaled products in terms of correlation and 10 out of 35 stations in terms of ubRMSD.

Table of abbreviations

AMI	Active Microwave Instrument
AMSR-E	Advanced Microwave Scanning Radiometer
AMSR2	Advanced Microwave Scanning Radiometer 2
ASCAT	Advanced Scatterometer
DVI	Differential Vegetation Index
ERS AMI	European Remote Sensing Active Microwave Instrument
ESA CCI	European Space Agency Climate Change Initiative
EVI	Enhanced Vegetation Index
GPP	Gross Primary Production
ISMN	International Soil Moisture Network
kNDVI	kernel Normalised Difference Vegetation Index
LAI	Leaf Area Index
LST	Land Surface Temperature
LST_{Night}	Night Land Surface Temperature
LST_{Day}	Day Land Surface Temperature
ΔLST	Difference in day and night surface temperatures
MIRAS	Microwave Imaging Radiometer using Aperture Synthesis
MWRI	Micro-wave Radiation Imager
NDVI	Normalised Difference Vegetation Index
PPI	Plant Phenology Index
R	Correlation Coefficient
SM	Soil Moisture
SMAP	Soil Moisture Active Passive
SMI	Soil Moisture Index
SMI_{mean}	Average Soil Moisture Index over the study area
SM_{cr}	Soil Moisture (Coarse resolution)
SM_{d}	Soil Moisture (Downscaled)
SMMR	Scanning Multi-channel Microwave Radiometer
SMOS	Soil Moisture Ocean Salinity
SSM/I	The Special Sensor Microwave Imager/Souder
T_{max}	Maximum temperature (Dry edge)
T_{min}	Minimum temperature (Wet edge)
T_{pixel}	Temperature of pixel
TCA	Triple Collocation Analysis
TMI	Tropical Rainfall Measuring Mission's Microwave Imager
ubRMSD	Unbiased Root Mean Square Deviation
VI	Vegetation Index
VTCI	Vegetation Temperature Condition Index

Table of Contents

List of Tables

List of Figures

1 Introduction

Soil moisture (SM) is simply defined as the volumetric content of water of the soil, which can stretch down to more than a metres depth (NIDIS, n.d.). Although for this study, evaluations are only limited to the upper 5 cm, as microwave remote sensing is only considered to represent the surface SM (Peng et al., 2015). SM plays a vital role in plant growth, acting as a plant's water source, a principal requirement for life. It also is an important factor in the exchange of heat and water between the surface and atmosphere through both plant transpiration and evaporation, effecting both water and energy cycles and by extension the climate (Civeira, 2019; ESA, n.d.). Thus monitoring SM has varying uses, whether its studying vegetation dynamics and observing changing climate effect, or evaluating flood risks and drought (Chifflard et al., 2018; Gałęzewski et al., 2021). Ideally, SM can be measured through ground instruments, which can obtain ground truths at a point scale in different depths and high temporal resolutions with relative ease (Peng et al., 2017). But these methods are insufficient as ground instruments are often sparse, limited and fail to represent areas around and between the ground instruments, which can vary greatly in SM due to surface heterogeneity such as topography, vegetation, or aspect (Fathololoumi et al., 2021). With the revolution of satellite remote sensing, it has become possible to estimate SM over large areas up to the global scale (Peng et al., 2017). Many different soil moisture products have been developed at varying spatial and temporal resolutions (Dorigo et al., 2017; Entekhabi et al., 2014; Jackson et al., 2012). However, the results are only as good as the data used, not only regarding its overall accuracy but also its resolution. One significant drawback of satellite-derived soil moisture (SM) products is their coarse resolutions, the European Space Agency Climate Change Initiative (ESA CCI) for example provides SM at 25 km resolution while the Soil Moisture and Ocean Salinity (SMOS) mission has a resolution ranging from 35-50 km. Such resolutions are unsuitable for local-scale studies, be it for crop modelling or water management applications (Peng et al., 2017, 2021). In addition, these soil moisture products are limited to very low penetration depths, only representing the top layer of the soil moisture, the surface soil moisture, whereas the soil moisture can extend metres below the surface to the root zone (NIDIS, n.d.).

Considerable efforts have been made to downscale coarse satellite SM to obtain a higher resolution product. Peng et al. (2017) summarized three main methods for increasing the spatial resolutions of satellite SM products. (1) The geoinformation method: Using ancillary data such as topography, soil attributes, and vegetation characteristics which is correlated with SM as parameters in the downscaling process. (2) The modelling method: which various models are based on geo-statistics to calculate statistics across different scales to describe the spatial distribution of a course SM product to model a finer SM product. (3) Satellite based methods: Using and combining the various advantages of different satellite sensors to achieve a more accurate product. Different algorithms under this category have been developed.

One commonly used method for spatial downscaling of SM with satellite-based methods is using the Optical/Thermal data. This method relies on the relationship of higher resolution ancillary data, such as land surface temperatures (LST) and vegetation indices (VI). Throughout the years various alterations have been made on these relationships. Initially, in 2002, Zhan et al, proposed using a polynomial fitting approach, in which a polynomial function was applied to LST and VI in addition to the surface albedo. Thus, a regression coefficient could be calculated from the coarser resolution data and then applied to the higher resolution data to obtain the downscaled SM. Later, in 2008, Merlin et al. proposed an alternative method to downscale a SMOS SM product in south-eastern Australia. It was a more physical based approach using variables more directly linked to SM, such as soil temperature, evaporative fraction and evaporation efficiency. This method is however computationally complex and is susceptible to uncertainties when estimating the SM variable through modelling. Kim and Hogue proposed a much simpler method in 2012, the UCLA method, in which a downscaling factor could be calculated from the LST-VI relationship as a function of LST, where it was calculated from the LST extremum for each VI value. This downscaling factor could then be applied to disaggregate the SM at a coarse spatial resolution to SM estimates at higher spatial resolution (Peng et al., 2017). Kim and Hogue (2012) also compared their method to the previously mentioned approaches on the AMSR-E SM product in southern Arizona and found that it performed better than the polynomial approach whilst producing similar results to Merlin et al.'s method. However, despite these methods showing increasing improvements and results they are still limited to the resolution of the higher resolution data, which in these cases are MODIS 1 km LST and VI data.

Recent efforts have been made to combat this, such as a study from 2017, which performed a polynomial downscaling approach over the Zoige Plateau using higher resolution (30 m) thermal infrared band and VI data provided by Landsat-5 to achieve promising results with the Normalised Difference Vegetation Index (NDVI) in addition to the Enhanced Vegetation Index (EVI) designed to limit the effects of the background soil. (USGS, n.d.; Zhao et al., 2017). This method is however limited by the low temporal resolution of the Landsat data. A further study by Xu et al. (2018) tried to solve this limitation by fusing the Landsat-8 data directly with MODIS data to maintain both high spatial and temporal resolutions which produced a daily SM product with 120 m spatial resolution which showed good performance with in-site measurements over Iowa (Xu et al., 2018). A limitation of these methods is that they used a linear fitting and assumed a simple relationship between the SM and auxiliary variables which could otherwise be more complex. To tackle this Mao et al. (2022) used the random forest machine learning method with auxiliary variables such as lagging SM as soil memory to combat the linearity of the LST and VI to downscale the SMAP SM product which resulted in good performance with in-situ measurements in The Pearl River Basin (Mao et al., 2022).

What these studies have in common, except for Zhao et al., (2017) is that they limit themselves to NDVI or EVI. However, there are many different VI available and using different VI as inputs could have important influence on the downscaled result as they are all unique and developed to tackle different issues. A previous study in Spain compared the spatial downscaling with NDVI and EVI and showed that EVI is more suitable than NDVI in estimating SM with a higher mean correlation coefficient (R) (Peng et al., 2015). More recently, EVI has been chosen over NDVI due to its various advantages in various downscaling processes with good results. For example in the downscaling of SMAP product with machine learning based approach in the Pearl River Basin (Zhang et al., 2022) and downscaling of the ESA CCI SM product in the Naqu area within the Tibetan Plateau (Zhu et al., 2023).

Since the introduction of EVI and NDVI, more complex and specialised VI have been developed resulting in improved performance, one of which is the Plant Phenology Index (PPI) introduced by Jin and Eklundh (2014) to improve performance in densely vegetated areas and limit the effects of snow, resulting in a product which has been shown to outperform both NDVI and EVI in high latitude areas and boreal forests. The kernel NDVI (kNDVI) is another recent VI product which has also shown to outperform NDVI by applying a kernel function to NDVI, to combat NDVI's saturation in dense vegetation and force a linear relationship between

the NDVI and the leaf area index (LAI), LAI being an indicator the amount of foliage in an area (Camps-Valls et al., 2021).

To the best of my knowledge, very few studies focused on testing with more complex or various VIs other than NDVI or EVI with optical and thermal satellite-based algorithms for spatial downscaling of gridded soil moisture products. Being a key factor in the determining how effect of evapotranspiration on LST, the VI is an important input to spatial downscaling algorithms, and different VIs have their strength and weaknesses and have varying suitability for different tasks, it is relevant and interesting to investigate how using different VIs would affect the downscaled results. This is relevant as various new VI products have been developed and released since NDVI and EVI which provide rich dataset to test. Therefore, this study aims to investigate the influence of using different VI on spatial downscaling of gridded SM products with the simplistic UCLA method with a Vegetation Temperature Condition Index (VTCI) as a scaling factor, as proposed by Peng et al. (2015), hereafter referred to as the VTCI based method. Using the VTCI based method, which has been shown to produce promising results in a variety of regions (Peng et al., 2016; Peng & Loew, 2017; Tian et al., 2019) this study's objective is to produce a more accurate SM product which is more suitable as a data source for analysis and modelling on a more local scale. Four different VI, namely the NDVI, EVI, PPI, and kNDVI will be used and compared to examine which can yield more accurate spatially downscaled SM estimates against the in-situ measurements from relatively dense network. This study will focus on SM in southern Europe and particularly the use of two SM networks within the International Soil Moisture Network (ISMN), the REMEDHUS network in Spain and SMOSMANIA network in southern France. Although this study uses previously defined downscaling methods, this study takes a novel approach as it: (1) uses more recent VIs such as PPI and kNDVI which haven't been used or evaluated for downscaling of SM, whilst other studies have been limited to more standard VIs such as NDVI and EVI (Peng et al., 2016; Zhang et al., 2022; Zhu et al., 2023); (2) focuses on the comparison and effects of the different VI inputs on the SM downscaling, opposed to other studies which have focused more on the methodology (Kim & Hogue, 2012; Tian et al., 2019); (3), uses a bigger study area and introduces the SMOSMANIA network in addition to the REMEDHUS network, allowing for more hydrological contrast and geographical variety in the study area and also allows for a comparison between to two different regions, whereas other studies have been limited to one region or few stations (Liu et al., 2021; Rostami et al., 2023). Specifically, this study will answer the following research questions:

1) How do different VI indices perform in the downscaling of SM and is there any VI which produces a more accurate product?
2) Do the different VI derived downscaling products give consistent results in different regions?
3) Are the downscaled SM products capable of providing better results than the coarse SM product?

2 Background

2.1 Satellite-based estimation of soil moisture

Satellites can estimate SM from the surface using microwaves (1-300 GHz) which are sensitive to the water content of the soil due to the poor transmission of microwaves through water which increases the dielectric constant (Seneviratne et al., 2010). A wet soil will thus emit less microwaves than a dry soil as the microwaves gets absorbed by the water in the soil. Satellites can measure these emitted microwaves either through a return signal from a transmitted wave pulse from the satellite (active) or as reflected radiation of the surface from an external source (passive) (Das & Paul, 2015). Active sensors tend to have a higher spatial resolution than passive sensors thanks to their larger antenna created by the Synthetic Aperture Radar (SAR) (NASA, 2020). In contrast, the passive sensors have the advantage of being more sensitive and generally having a higher temporal resolution of daily measurements, see Table 1 (Entekhabi et al., 2014; Peng et al., 2017).

These sensors also vary in respect to what specific wavelengths they use. Wavelength at lower frequencies are in general more suitable for SM measurements due to their increased surface penetration power. For instance, X-band frequencies (8-12 GHz) tend to only interact with the top of the canopy whilst lower frequency C-bands (4-8 GHz) penetrate further into the canopy. The L-band (1-2 GHz) is the preferred band as it manages to reach and reflect from the soil surface, providing more information on the soil profile (Das & Paul, 2015).

In previous years, SM measurements have been conducted with a variety of sensors onboard different satellites. The passive Scanning Multichannel Microwave Radiometer (SMMR) was launched in 1978 onboard the Nimbus-7 satellite capable of measuring microwave radiation at

6.6-37 GHz and providing daily measurements at 25 km resolution up until 1987 (Guha & Lakshmi, 2004). Roughly half a month later, the Special Sensor Microwave Imager (SSM/I) passive sensor was launched onboard the DMSP-F8 satellite, increasing the measurable microwave range to 19-85 GHz, providing daily measurements at 12.5-25 km resolution and until 2009 (National Snow and Ice Data center, n.d.). The sensor was however further improved in 1997 onboard the Tropical Rainfall Measuring Mission (TRMM) in which a pair of additional 10.7 GHz channels were added to the sensor, now named The TRMM Microwave Imager (TMI) capable of obtaining daily measurements at 5-45 km resolution (NASA, n.d.). Other notable passive sensors include the Advanced Microwave Scanning Radiometer for EOS (AMSR-E), the WindSat sensor, the Advanced Microwave Scanning Radiometer 2 (AMSR2) and the Micro-wave Radiation Imager (MWRI) (Minnett, 2019; National Satellite Meteorological Center, n.d.; OSCAR, n.d.).

For active sensors, The Active Microwave Instrument (AMI) was launched in 1991 onboard the European Remote Sensing Satellite 1 (ERS-1), providing wavelength measurements at 5.3 GHz (C-Band) every 3 days at 50 km resolution up until 2000 due to a technical failure but was then replaced by ERS-2 from 1995 till its retirement in 2011 (Attema, 1991; ESA, n.d.). However, before then, in 2006, the Advanced Scatterometer (ASCAT) was launched onboard the MetOp-A satellite, succeeding the AMI, providing measurements at 5.3 GHz from 2006 until 2021. Since then MetOp-A, MetOp-B and MetOp-C have also been launched with the ASCAT sensor providing measurements from 2012 and 2018 respectively providing measurements every 1.5 days at 12.5 – 50 km resolution (EUMETSAT, 2020a, 2020b).

Most of these sensors provide very high frequency measurements but the area is lacking in lower end of the spectrum, not having the lower frequencies needed for optimal ground penetration and soil moisture retrieval (< C – Band) (Das & Paul, 2015). To combat this, the first dedicated SM mission, specifically designed to measure SM was launched in 2009, The Soil Moisture and Ocean Salinity mission (SMOS), using 1.4 GHz (L-Band) to measure surface SM with a spatial resolution of 35 km, every 2.5-3 days (Parrens et al., 2016). The SMOS has been used in various studies and has shown to have good accuracy with field observations (Jackson et al., 2012; Yang et al., 2016). It has however been shown to be very sensitive to noise from radio frequency interference.

Alternatively, the European Space Agency Climate Change Initiative (ESA CCI) SM product was introduced in 2010 and has proven itself as an suitable soil moisture index but is also limited in having a very coarse spatial resolution of 0.25° (28 km). The ESA CCI SM takes advantage of both passive (SMMR, SSM/I, TMI, and AMSR-E) and active (ERS AMI and ASCAT) sensors and combining them to produce a more accurate product (Dorigo et al., 2017; Peng et al., 2016) which has shown to have a better performance over SMOS in humid areas in Michigan, in terms of ubRMSD (X. Xu & Frey, 2021a). The ESA CCI SM good performance could be attributed to its use of the Triple Collocation Analysis (TCA) method in combining the different SM products. The TCA limits the amount errors of the combined products by calculating the covariance between them to retrieve their respective errors. The errors of each product can then be used as weights to combine the products on a per-pixel basis, where a higher weight is assigned to lower errors (Dorigo et al., 2017; Gruber et al., 2016).

More recently, the Soil Moisture Active Passive (SMAP) mission was launched in 2015, using the L-Band akin to SMOS, but based on the same foundation as ESA CCI of using concurrent measurements from both an active and passive sensor (Entekhabi et al., 2014), but differing in the sense that both measurements belong to the same satellite, providing measurements every 9 days with 9 km resolution. A study comparing SMAP and SMOS SM products over different landscapes in Africa, showed the advantages of SMAP, having both a higher correlation and lower error than SMOS and ASCAT products (Mousa & Shu, 2020). Compared to ESA CCI, SMAP showed higher correlation but ESA CCI achieved a higher absolute accuracy with a lower average ubRMSE (X. Xu & Frey, 2021b).

However, in spite of these three SM products, SMOS, SMAP and ESA CCI showing great promise and accuracy, one significant drawback of these products are their coarse resolutions which are unsuitable for analysis on a local scale, whether it be for crop modelling or water management applications (Peng et al., 2017). In order to support regional studies effectively, it is crucial to utilize suitable spatial downscaling algorithms to disaggregate such SM products at coarse resolution to SM estimates at higher spatial resolution.

Table 1. An overview of the different satellite sensors along with their respective frequencies and temporal range (Attema, 1991; Entekhabi et al., 2014; ESA, n.d.; EUMETSAT, 2020a, 2020b; Guha & Lakshmi, 2004; Minnett, 2019; NASA, n.d.; National Satellite Meteorological Center, n.d.; National Snow and Ice Data center, n.d.; OSCAR, n.d.).

Sensor	**Satellite**	**Frequency (GHz)**	**Spatial resolution (km)**	**Temporal resolution**	**Temporal Range (years)**	**Sensor Type**
SMMR	Nimbus-7	6.6-37	25	Daily	1978-1987	Passive
SSM/I	DMSP-F8	19-85	12.5-25	Daily	1987-2009	Passive
TMI	TRMM	10.7-85	5 – 45	Daily	1997-2015	Passive
ASMR-E	Aqua	6.9-89	5.4–56	Daily	2002-2011	Passive
WindSat	Coriolis	6.8-37	25	Daily	2003-2021	Passive
AMSR2	GCOM-W1	6.9-89	3-62	2 days	2012-	Passive
MWRI	FY-3B	19.6-150	11-40	Daily	2010-2020	Passive
MIRAS	SMOS	1.4 (L-Band)	35-50	2.5-3 days	2009-	Passive
Radar/ Radiometer	SMAP	1.2-1.3 (L-Band)/ 1.4 (L-Band)	9	2-3 days	2015-	Active/ Passive
AMI	ERS-1/2	5.3 (C-Band)	50	3 days	1991-2000	Active
ASCAT	MetOp-A/ MetOp-B/ MetOp-C	5.3 (C-Band)	12.5 – 50	1.5 days	2006- 2021/ 2012-/ 2018-	Active

2.2 Optical and thermal satellite-based methods for spatial downscaling of soil moisture products

There are various ways in which downscaled SM (SM_d) has been obtained with optical and thermal satellite-based methods. One of which is a triangular method, in which SM is calculated from the VI, LST and a regression coefficient that are implemented into a second-order polynomial regression formula in which the SM can be calculated. This equation can be rewritten to isolate and calculate the regression coefficient using the known SM of the coarser SM product. The regression coefficient can then be reapplied to the higher resolution VI and LST to calculate the downscaled SM (Kim & Hogue, 2012). This method is however highly dependent on the accuracy of the coarser scaled SM product (SM_{cr}), in which any errors or poor accuracy in the SM_{cr} will result in a poor polynomial fitting which further produces significant uncertainties to the SM_d products (Kim & Hogue, 2012).

Another study by Merlin et al. (2018), used a similar method as described above but suggested using additional SM parameters and micrometeorological and atmospheric observation, such as soil moisture capacity, evaporation resistance, vegetation skin temperatures and fraction covers (Merlin et al., 2008). A study in 2012 in Arizona has shown that this method produced good results, having both higher correlations and lower ubRMSD than the triangular method (Kim & Hogue, 2012). However, this method puts more weight on the LST than the VI, which becomes a limitation and disadvantage when LST may not be representative of the soil, such as when LST may be dominantly influenced by altitude, geographic location, etc. (Kim & Hogue, 2012). In addition, it is a complex method, requiring more inputs which may depend on soil types, boundary conditions, etc.

A simpler method was proposed by Kim and Hogue (2012), the UCLA method, which unlike the triangular method is not based on a regression approach, nor does it require additional information on soil properties, surface micrometeorological or atmospheric observations akin to the method proposed by Merlin et al. (2008). The UCLA method instead relies on retrieving a scaling factor from the LST-VI relationship which can then be normalised by average SM value and then applied as a scaling factor to the coarser SM product, see Equation 1.

$$SM_d = SM_{cr} \times \left(\frac{SM_{VI-LST}}{\overline{SM}_{VI-LST}}\right) \quad (1)$$

Where, $SM_{VI\text{-}LST}$ is the scaling factor, calculate from the LST of each VI value and $\overline{SM}_{VI\text{-}LST}$ is the mean of the scaling factor values within the overlaying coarser scaled pixel. SM_{cr} is the coarser resolution SM and SM_d is the downscaled SM product (Kim & Hogue, 2012). The calculation of the $\overline{SM}_{VI\text{-}LST}$ can be seen on Equation 2, where *n* and *m* are the number grids of the SM_d product within the *i*th row and *j*th column of the SM_{cr} product.

$$\overline{SM}_{VI-LST} = \frac{1}{mn}\sum_{i=1}^{n}\sum_{j=1}^{m} SM_{VI-LST\,ij} \qquad (2)$$

A comparison to the aforementioned downscaling methods showed that both Merlin's method and UCLA methods performed better than the triangular method, with UCLA only having a slightly higher RMSE value than Merlin's method. The UCLA however has the advantage of needing less inputs and being computationally more efficient (Kim & Hogue, 2012).

2.2.1 Scaling factor

A prominent scaling factor which has been used in a variety of evaluations is the Vegetation Temperature condition index (VTCI) (Tian et al., 2019), first developed in 2004 as a way to measure drought in which a lower VTCI values correlates to a higher degree of drought (Wan et al., 2004). VTCI is defined with the following Equation 3:

$$VTCI = \frac{T_{max} - T_{pixel}}{T_{max} - T_{min}} \qquad (3)$$

where, T_{max} an T_{min} are the maximum and minimum temperatures for all pixels within a specified VI interval and T_{pixel} is the temperature of a specific pixel. T_{min} represents the wet edge, or lower limit where there is no water restriction on plant growth. In contrast T_{max} represents a dry edge where plants are under dry condition. Thus, from Equation 3, we can calculate a value VTCI value ranging from 0 to 1, signifying the level of drought and SM (Wan et al., 2004).

2.2.3 Triangular feature space

A fundamental element of optical and thermal based downscaling methods is the triangular feature space, which describes the relationship between the vegetation of a pixel and its temperature (Garcia et al., 2014). The space derives its name from the triangular/trapezoidal pattern that appears when pixel values are plotted over an area which follows the following criteria (Garcia et al., 2014) : (1) Enough hydrological contrasts (from wet to dry soils) (Garcia et al., 2014) ; (2) For a given VI, the variations in LST reflect variations in SM and then the partitioning of sensible and latent heat fluxes, assuming the other factors such as the available energy to the surface, air temperatures and aerodynamic resistance are the same (Garcia et al., 2014).

The pattern is limited by two boundaries which form the triangle/trapezoid, *the wet edge*, a zone of max evaporation which represents the minimum temperature for each VI interval and *the dry edge*, a zone of no evaporation which represents the maximum temperature for a given VI interval (Peng et al., 2017), see Figure 1.

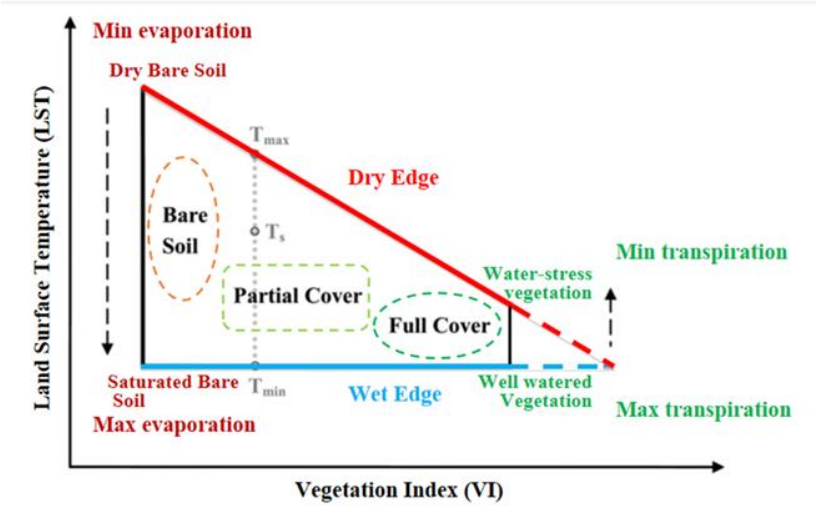

Figure 1. Diagram of the triangular (trapezoidal) space between land surface temperature (LST) and vegetation index (VI). (Figure reprinted and modified from Li et al., 2009, Peng et al., 2017 and Zhao et al., 2022).

There are various ways in which the wet and dry edges are defined, the simplest method, used by Peng et al. (2015) is to use the maximum and minimum temperatures for each VI interval, determined by the dry and wet edges respectively and applying them to every pixel within said interval.

An alternative study by Garcia et al. (2014) investigated using quantile regression to define the dry edge based on the value of the upper quantiles with a fixed wet edge value, either as a constant 0 or the mean of all values. The study compared the effect of different upper quantiles and wet edges values. There results determined that using a 95% and 99% upper quantile for the dry edge and a constant value 0 for the wet edge showed best results with R value of ~0.8 with in-situ measurements. The study however did not compare this method with the simpler method used by Peng et al. (2015).

2.3 Vegetation indices

Vegetation indices (VI) can be defined as the combination of different surface reflectance wavelengths in order to highlight or quantify vegetation properties. The reflected surface wavelengths are highly related to the vegetation as it absorbs visible light (400-750 nm) due to photosynthesis and thus the ratio of reflected visible to near infrared (0.75-1.3 μm) wavelength is affected, allowing us to differentiate and quantify the amount of vegetation in a simple manner. The VI is an important tool in vegetation monitoring, being a key indicator of vegetation conditions, cover, foliage, and phenology, as well as estimating various processes such as evapotranspiration and primary production (Jin & Eklundh, 2014). Thus, using radiometric measurements VIs can be created to indicate the amount of vegetation on a per-pixel basis (Pettorelli, 2013b). Various studies have compared the performance of different VIs and shown the potential of using different VI to tackle varying issues (Camps-Valls et al., 2021; Jin & Eklundh, 2014; Tiruneh et al., 2022). Based on literature review, this study focused on four VIs. Firstly, the Normalised Difference Vegetation (NDVI) was chosen for its simplicity and popularity, serving as an important benchmark for comparisons of the other VIs. Secondly, the Enhanced Vegetation Index (EVI) was chosen because of its popularity and its ability to produce good results in a variety of environments, limiting the effects of both soil and atmospheric background noise. Thirdly, the Plant Phenology Index was chosen, not only because of its suitability in dense vegetation and linearity LAI but also because despite showing relatively good performance, a limiting amount of studies have been conducted to further evaluate the index. Lastly, the kernel NDVI (kNDVI) was chosen as it is a relatively novel index and a few studies have used it for evaluation. Furthermore, it is a very simple index which can be derived from NDVI, conserving its simplicity but also being more suitable for denser vegetation.

2.3.1 Normalised Difference Vegetation Index

The most widely used index is the Normalised Difference Vegetation Index (NDVI), first introduced in 1974 (Rouse et al., 1974; Xiang et al., 2000). NDVI quantifies vegetation based on the difference between the vegetation reflectance of the near infrared (NIR) wavelengths and its absorption of the visible Red wavelengths (Pettorelli, 2013a), see Equation 4, where NIR and Red are the reflectance of the near infrared and visible red wavelengths respectively. The simplicity of the NDVI and the availability of the NIR and Red bands have made NDVI a popular choice of index. It is a ratio-based index which makes it less susceptible to signal variations from varying laminations, topography or other viewing conditions (Fensholt et al., 2006). Although NDVI's popularity and simplistic approach may make it seem like an obvious choice of VI, it does have its disadvantages. As a ratio-based index, it is nonlinear with LAI, making it less sensitive and highly saturated to dense vegetation (Huete et al., 2002) in addition to being very sensitive to aerosols in the atmosphere and underlying soil (Pettorelli, 2013a).

$$NDVI = \frac{NIR-Red}{NIR+Red} \qquad (4)$$

2.3.2 Enhanced Vegetation Index

The Enhanced Vegetation Index (EVI) is another notable index designed to limit the effects of the atmosphere and background soil (Chuvieco, 2016). The foundation of the EVI is the implementation of the Blue band, which suffers from the same atmospheric impacts as the Red band and can thus be used to cancel out or limit any of its effects. A soil adjustment factor (*L*) is then further implemented to limit the effects of the soil background(Huete et al., 2002).

EVI also considers coefficients C_1 and C_2 which are aerosols resistance terms which allow the Blue band to correct for aerosol influences in the Red band as well as a gaining factor (*G*) to boost the sense of the signal, see Equation 5. For EVI, $C_1 = 6$, $C_2 = 7.5$ and $G = 2.5$ (Chuvieco, 2016; Huete et al., 2002).

$$EVI = G \times \frac{NIR-Red}{NIR+C_1 \times Red-C_2 \times Blue+L} \qquad (5)$$

EVI does have a drawback which is that it is dependent on the Blue band, which makes monitoring of EVI over a long range in time limited as the Blue band was only implemented

in MODIS satellite sensors in 2000 (Jiang et al., 2008). EVI2 was thus created to tackle this issue (Jiang et al., 2008). By assuming the visible bands, Blue and Red in this case, are highly correlated with each other than the Blue band can be substituted for the Red band, using a coefficient *c*, see Equation 6.

$$Blue = \frac{Red}{c} \quad (6)$$

Thus, we get a new equation for EVI2 which uses only the Red and NIR bands, see Equation 7.

$$EVI2 = G \times \frac{NIR - Red}{NIR + \left(6 - \frac{7.5}{c}\right) Red + 1} \quad (7)$$

2.3.3 Plant Phenology Index

A study in 2014 introduced the Plant Phenology Index (PPI), a new VI to counter prior VI's sensitivity to dense vegetation and non-linearity with LAI, the foundations of which is that LAI is the most visible variable in a plants phenological cycle. This is important, especially in boreal areas, where green biomass renewal rate is slow, and reflectance will be affected by snow (Jin & Eklundh, 2014).

Akin to NDVI, PPI is calculated from Red and NIR reflectance, however PPI is based on a modified Beer's law which also takes into account the relationship between the LAI and canopy reflectance, see Equation 8 (Jin & Eklundh, 2014).

$$PPI = -K \times ln \frac{(M - DVI)}{M - DVI_s} \quad (8)$$

Here DVI represent the difference in Red and NIR reflectance, whilst more specifically the DVI_s is the difference in Red and NIR reflectance of the soil. M is the maximum DVI value per pixel (canopy maximum) from all available data ranging from 2000 to 2022. K represents a gaining factor which is also dependant on the sun zenith angles, the diffuse fraction of solar radiation and leaf angular distribution (Jin & Eklundh, 2014).

PPI has been found to perform better than EVI and NDVI in snowy and northern regions to determine start of seasons. Similarly, PPI has shown stronger correlations with GPP ground

measurements than both NDVI and EVI in forest covering Sweden and Finland. Additionally, the same study showed that PPI is not affected by saturation of dense vegetation like the other VIs. The way in which PPI handles snow and saturation can be very important in SM estimation, especially in areas of dense vegetation, such as forests but also areas prone to snow cover such as northern latitudes and high elevation areas (Jin & Eklundh, 2014).

However, a disadvantage of the PPI is that it seems to be more sensitive to noise then NDVI and EVI during the peak of the growing seasons and at high LAI values but does however display more robustness during the seasonal transition periods. This can be explained by the reflectance being insensitive to LAI in the growing season, thus resulting in NDVI and EVI, not being as affected as they are not linear with LAI (Jin & Eklundh, 2014).

2.3.4 Kernel Normalised Difference Vegetation Index

The kernel Normalised Difference Vegetation Index (kNDVI) was introduced to conserve the simplicity of the NDVI but combat its issues in dense vegetation. kNDVI uses a kernel function to solve the non-linearity of NDVI with LAI, which in turn limits the saturation effects of dense vegetation (Camps-Valls et al., 2021). A radial basis function, k, reproducing kernel is used to measure similarities between NIR and red bands, see Equation 9 where x and x' represent the NIR and red bands respectively and σ represents the notion of distance between the NIR and red bands (Camps-Valls et al., 2021), see Equation 9.

$$k(x, x') = exp\left(\frac{-(x-x')}{2\sigma}\right)^2 \qquad (9)$$

This equation can be further simplified by assigning the average distance between NIR and Red bands as σ, i.e., σ = 0.5(NIR + Red) theoretically making the index more adaptive to each pixel, resulting in a simplified Equation 10 (Camps-Valls et al., 2021).

$$kNDVI = \tanh\left(NDVI^2\right) \qquad (10)$$

An evaluation on 169 FLUXNET stations around the world found that not only does kNDVI show stronger correlation than NDVI with GPP measurements but it also outperforms NDVI in all applications in all biomes and climate zones and is more resistant to saturation and noise.

This can be important for estimating SM for the same reason as the PPI, however kNDVI has the advantage of having a much simpler approach (Camps-Valls et al., 2021).

3 Study area

Two study areas were used for the evaluation of the downscaled SM. Study area 1 is located in northern Spain and covers the area of the REMEDHUS network, the same study area used by Peng et al (2015) and thus this facilitates a direct comparison of our results. The region is relatively flat and has dry and warm summers and wet and mild winters due to its semiarid Mediterranean climate. Study area 2 covers a larger area, spreading from southern France to Italy and up to Austria, Switzerland, and southern Germany where there is a lot of contrast in soil moisture surrounding the Alps. The network, SMOSMANIA that was used for the evaluation in study area 2 is in southern France. Sharing a similar climate to its southern counterpart, the region surrounding the SMOSMANIA network gets mild wet winters and dry warm summers from the Mediterranean, but experiences wetter summer as the area extends westwards to a more Oceanic climate. Both study areas, along with their measurement stations can be seen on Figure 2. An overview of the stations used and their landcover is presented in Table A1 in the Appendix.

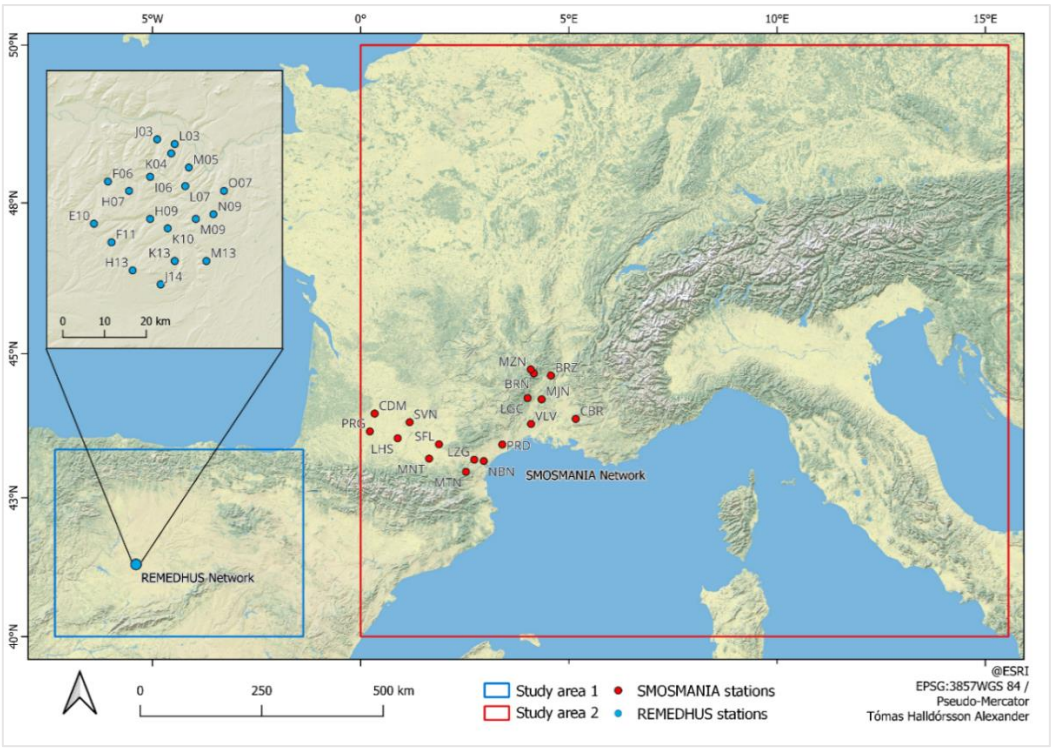

Figure 2. Locations of the two study areas and in-situ soil moisture measurements from the ISMN stations.

4 Data

4.1 Satellite data

The data used in this study include LST and VI data acquired from the Moderate Resolution Imaging Spectroradiometer (MODIS) sensor onboard the Aqua and Terra satellites, providing daily measurements globally at 0.25° (~28 km), 0.5° (~55km) and 1 km spatial resolutions. The MODIS MOD13A2 product was used to obtain the NDVI and EVI data, providing 16-day VI data at 1 km resolution. The 16-day data is composited from 8-day data in which each pixel value represents the best value, in terms of cloud cover, atmospheric condition and viewing angle, over the 8-day period. In a more straightforward approach, the LST was obtained from the MOD11A2 MODIS product, in which every 8 days is averaged into 8-day composites for both day and night temperatures at a 1 km resolution. PPI obtained from MCD43 NBAR MODIS product at 500 m resolution was provided by Hongxiao Jin, its creator and researcher at Lund University. Both the VI and LST data were collected for both MODIS tiles H17V8 and H18V8, covering study areas 1 and 2 respectively, spanning January 1st, 2010, to December

31st, 2011, for study area 1, and from January 1st, 2018, to December 31st, 2020, for study area 2.

For the lower spatial resolution SM, the ESA CCI SM v07.0 COMBINED product from ESA CCI was used, created by a combination of both active (ERS AMI and ASCAT) and passive (SMMR, SSM/I, TMI, AMSR-E) satellite products, resulting in a daily 0.25° spatial resolution SM product with a 5 cm observation depth and global coverage. As the ESA CCI SM product only has global coverage, the data was extracted for the previously mentioned dates, regardless of the study areas.

4.2 In-situ soil moisture measurements

For the purpose of evaluation, in-situ SM measurements were retrieved from the ISMN, providing a harmonised database of SM across the globe in cubic metres of water per cubic metre of soil (m^3/m^3) at varying depths. Two ISMN networks were used for the evaluation, the SMOSMANIA and REMEDHUS networks. The REMEDHUS network contained 24 stations. For this study 7 stations were omitted as they did not cover the study period, either partly or fully. SMOSMANIA network contained 21 stations, all station matched the study period, but 3 stations had to be removed as they were not covered by the study area. Despite the harmonisation efforts of the ISMN, networks do differ in their measurement sensors. The REMEDHUS stations, for example, use the Stevens Hydra Probe sensor by Stevens Water Inc. whilst SMOSMANIA stations use the ThetaProbe ML3 and ThetaProbe ML2x sensors by Delta-T Devices. These sensors are however comparatively very similar, all having a sensing radius of 3 cm around the sensor and accuracy of ± 0.01 m^3/m^3. For this study, hourly SM data tagged as "GOOD" quality at a depth of 5 cm for 16 stations within the REMEDHUS network and 18 stations within the SMOSMANIA network were used, covering both study areas. Data was extracted in accordance with their respective study areas and previously mentioned dates.

The data used, their temporal and spatial resolution along with other information are summarised in Table 2. An overview of ISMN station used for the evaluation is listed in the Appendix, along with the dates used.

Table 2. Overview of data used along with their spatial and temporal resolutions and coverage (Data obtained from https://ladsweb.modaps.eosdis.nasa.gov/search/ and https://esa-soilmoisture-cci.org/).

Data	Product	Spatial resolution	Temporal resolution	Spatial Coverage	Temporal Coverage
ESA CCI	Soil moisture	0.25°	Daily	Global	2010 - 2011 & 2018 - 2020
MOD11A2	LST_{day} & LST_{night}	1 km	8-day average	MODIS tiles H18V4 & H17V4	2010 - 2011 & 2018 - 2020
MOD13A2	NDVI, EVI & kNDVI	1 km	16-day composites	MODIS tiles H18V4 & H17V4	2010 - 2011 & 2018 - 2020
MCD43 NBAR	PPI	500 m	Daily	MODIS tiles H18V4 & H17V4	2010, 2011 & 2018 - 2020

5 Methodology

The downscaling of the ESA CCI SM for this study is partly based on a previous study from Peng et al. (2015) for downscaling SM in northern Spain, using the VTCI based downscaling method proposed by Kim and Hogue (2012) with VTCI as a scaling factor. In addition, the wet and dry edges are simply defined by the extremum of the temperature for each VI interval, as opposed to the upper and lower quantiles, as proposed by Garcia et al (2014) as it did not show any advantage during the initial testing for this study.

5.1 Data harmonisation

Before any processing and calculations can be done, all datasets had to be harmonised so both their projections and temporal resolutions were aligned and converted into GEOTIFF format. The NDVI, EVI and LSTs were extracted from their relative Hierarchical Data Formats (.hdf) using the HDF-EOS to GEOTIFF conversion tool (HEG) which converted the data formats to GEOTIFFs as well as reprojected it from its sinusoidal projection to a geographical projection to correlate with the ESA CCI soil moisture product. From the resulting NDVI GEOTIFF, the kNDVI could be calculated using Equation 10. But first all negative values had to be masked and reclassified so they would not get converted into positive values. Daily ESA CCI SM was downloaded from an FTP server as NetCDF files in a geographic projection. The

MakeNetCDFRasterLayer function within the *arcpy* module in python was used to convert the ESA CCI SM from NetCDG to GEOTIFFs whilst conserving its projection. To convert the PPI data, the MATLAB files were read into python using the *scipy* module to extract the PPI data as arrays. Which were then converted into rasters with the *arcpy NumPyArrayToRaster* function using the lower left corner of the H18V04 tile and pixel size as parameters and then defining the projection to match the ESA CCI SM product. A bilinear resampling approach was then applied to the PPI data to upscale it to the same resolution as the other VI and LST.

After all data sets had been spatially aligned, excluding the coarser resolution, they all had to be temporally aligned. The EVI, NDVI and kNDVI have a temporal resolution of 16 days. This acted as the temporal limit, so all other datasets were upscaled to a 16-day resolution. As is the case with PPI and ESA CCI SM, data for every 16th day snapshot was extracted and used, averages and compositions were not calculated for this daily data so that a snapshot per snapshot comparison could be conducted with in-situ measurements. In addition, due to that complicated methods in which the 16-day composites are calculated, compositing the daily data by simple averaging would not produce a fair equivalent. But in the case for the LSTs, a dataset including 8-day averages at 8-day intervals was used to combat the limiting amount of data provided by the alternative daily LST snapshot dataset. So, every other dataset, i.e., 8-day averages at 16-day intervals was used.

In the case of temperatures, LST can vary greatly over large areas time of day, locality and elevation, making it liable to cause uncertainty in the triangular feature space. To account for these various studies have made efforts to combat this using the difference in day and night LST to obtain a more relative temperature. Their results have shown improved results in the downscaling of both the ESA CCI SM product in northern Spain as well as in southwestern China (Peng et al., 2015, 2016). The same approach was used in this study, using day and night LST from the MOD11A2 product and subtracting them using Equation 11.

$$\Delta LST = LST_{day} - LST_{night} \quad (11)$$

Now that all datasets were spatially and temporally harmonised and have been scaled, a further processing could commence.

5.2 Vegetation Temperature Condition Index

In order to calculate the Vegetation Temperature Condition Indices (VTCI), each VI raster for each day was plotted against the corresponding ΔLST raster. The VI and ΔLST rasters were converted into arrays using the *numpy* module and the subsequently turned into lists which were then plotted together, one point for each pixel within the study area for each day. For study area 2, this amounted to a maximum of 287.832 points whilst for study area 2 it amounted to a maximum of 1.122.368 point, the amount of points plotted were then limited to the amount of pixels available with valid data. From the plot created, showing a triangular or trapezoidal relationship between ΔLST and VI, the upper (wet edge) and lower (dry edge) boundaries, see Figure 1, could be calculated. The edges were calculated by extracting the highest and lowest ΔLST values for each VI interval. In this case the interval was defined as 0.05. The highest and lowest ΔLST values were then added to a separate list along with their corresponding VI values. Using the *polyfit* function within the *numpy* module the slope and y-intercept of the best fitting linear line for each edge could be calculated. As opposed to Peng et al. (2015) study, where the wet edge is fixed for all VI intervals, here the wet edge is dynamic. It is assumed that the rate of evaporation is related to the amount of vegetation, thus the change in vegetation should have an impact on the temperature. This approach has been shown to give promising results, having been used in the downscaling of ESA CCI SM in western Iran, achieving correlations of roughly 0.7 with in-situ measurements (Rostami et al., 2023).

With the edges defined, the VTCI could be calculated based on the VI values. For each pixel, its VI value was checked, and its interval determined. The VTCI was then calculated by subtracting its corresponding ΔLST from the wet edge value for each interval and then dividing it by the difference in wet edge and dry edge values, using Equation 3, but substituting the daily LST value with ΔLST. These VTCI values were then added to a new empty array. In the case in which a VI value does not belong to an interval, the value was added to the new VTCI array as NODATA. Using the *NumPyArrayRaster* the VTCI arrays were converted into GEOTIFFs using the lower left corner and the cell sizes of the original raster as parameters. The results being VTCI rasters for each type of VI at 16-day intervals. With the VTCI serving the purpose as a scaling factor to apply to the coarse resolution ESA CCI SM product.

5.3 Spatial downscaling

Each VTCI raster for each date and VI was applied to the ESA CCI SM product of the same date. First the ESA CCI SM was resampled to the same spatial resolution as the VTCI so a pixel-on-pixel calculation could be processed. The downscaling was done by multiplying the pixel value of the VTCI raster with the ESA CCI SM value of its corresponding pixel and then dividing it with the average VTCI values within the boundaries of the overlaying coarser resolution pixel, see Equation 1, where $SM_{VI\text{-}LST}$ is replaced by VTCI and SM_{cr} is the ESA CCI M product to achieve the downscaled SM ($SM_{d)}$.

5.4 In-situ soil moisture measurements from ISMN stations

The ISMN stations measure SM at an hourly interval. Thus, to match their data with satellite observations, their measurements averaged to obtain the mean daily SM, a similar approach to that of Zhu et al. (2023) who used said approach to match 30 min measurements to daily averages. For this study measurements were extracted from 00:00 to 23:00 for every day and averaged to obtain the daily mean. In order to limit the effects of absence of data, the average was calculated by summing up all the measurements and dividing by the amount of hours with measurements, as opposed to simply dividing by the amount of hours in the day. Subsequently, to match with the lower temporal resolution satellite data, every 16th value was extracted to obtain a dataset containing 16-day in-situ data from the ISMN stations.

To obtain the pixel-based SM of the 16-day SM_d products corresponding to each station the *Sample* function within the *arcpy* module was used. Because of the low radius (3 cm) of in-situ measurements, only the overlaying pixel, 1 km for SM_d and 25 km for SM_{cr}, was sampled. This was done for all SM products. The resulting point sampled SM products for each station were then written into a text file which could then be read into python and formatted as separate lists for each different SM product.

5.5 Evaluation

The *pytemso* python toolbox was used to evaluate the SM_d products with the ISMN stations, using the listed values of the downscaled SM product and in-situ measurements. Measurements were only compared for days in which data was available for all products, thus new lists were created for each VI which only contained data for dates which had data for all the different VI.

These lists of values, one for each SM product were then evaluated against the in-situ measurements list using two functions within the *pytemso* toolbox, The *ubrmsd* function which calculated the unbiased root-mean-square deviation (ubRMSD) in m^3/m^3 and *pearsonr* function which calculated the unitless Pearson correlation coefficient (*R*). The ubRMSD, has been widely used in SM evaluations as it can reflect SM anomalies independent of bias which may be caused seasonal changes in SM, elevation or surface roughness, see Equation 11 where *x* and *y* and are predicted and observed values respectively and $\bar{x}$ and $\bar{y}$ are there means (Entekhabi et al., 2010; Peng et al., 2015; Zhang et al., 2022). Likewise, the *R* value is also a widely used metric for evaluation of SM as it measures the strength of the linear relationship between predicted and observed values, ranging from -1 to 1 where the correlation increases/decreases as it deviates from 0, see Equation 12 where x and y are the predicted and observed values respectively and *n* is the amount of pairs (Entekhabi et al., 2010; Peng et al., 2015; Profillidis & Botzoris, 2019).

$$ubRMSD = \sqrt{((x - \bar{x}) - (y - \bar{y}))^2} \qquad (11)$$

$$R = \frac{n(\sum xy) - (\sum x)(\sum y)}{\sqrt{[n\sum x^2 - (\sum x)^2][n\sum y^2 - (\sum y)^2]}} \qquad (12)$$

The SM_d products were evaluated against the 17 stations within the RHEMEDUS network and 18 stations in the SMOSMANIA network. *R* and ubRMSD values of each station were calculated as well as the simple mean across all stations for each network. In addition, a weighted mean of *R* was also calculated using the variance of each station as a weighing factor, where a higher weight is attributed to stations with lower variance. This was done so that low accuracy and potentially erroneous stations would have a limited impact on the results. Additionally, all SM products were plotted with the in-situ ground measurements to look at temporal patterns and overall fit.

To compare the spatial patterns of the different SM_d products, the SM_d products were visualised on maps, along with the LST and $SM_{cr\text{-}ESACCI}$, for both study areas on the same day. By doing this the SM_d products could be visually compared over a larger area and the effect of LST and SM_{cr} visualised. In addition, their temporal patterns were analysed by the plotting a time series of the SM_d products along with the SMcr and in-situ measurements. Through the time series, the performance of the SM_d could be compared visually with the in-situ measurements and

SM_{cr} to see how they match with their temporal variations. So not only could their performance be evaluated against the in-situ measurements, but also the original SM_{cr} product.

6 Results

6.1 LST-VI relationships

The LST-VI feature spaces were calculated at 16-day intervals for each VI. Figure 3 shows the different features spaces for the same day in 2018 produced by the 4 different VIs. From these figures we can see that the NDVI showed more of a square shape whilst the alternative VIs, such as EVI and kNDVI, showed a better resemblance to a trapezoid and PPI showing a very distinct sharp triangular shape. The NDVI and kNDVI samples also seemed to be denser at the higher end of the VI spectrum whilst EVI, tended to be denser in the middle and PPI had the highest density in the lower end.

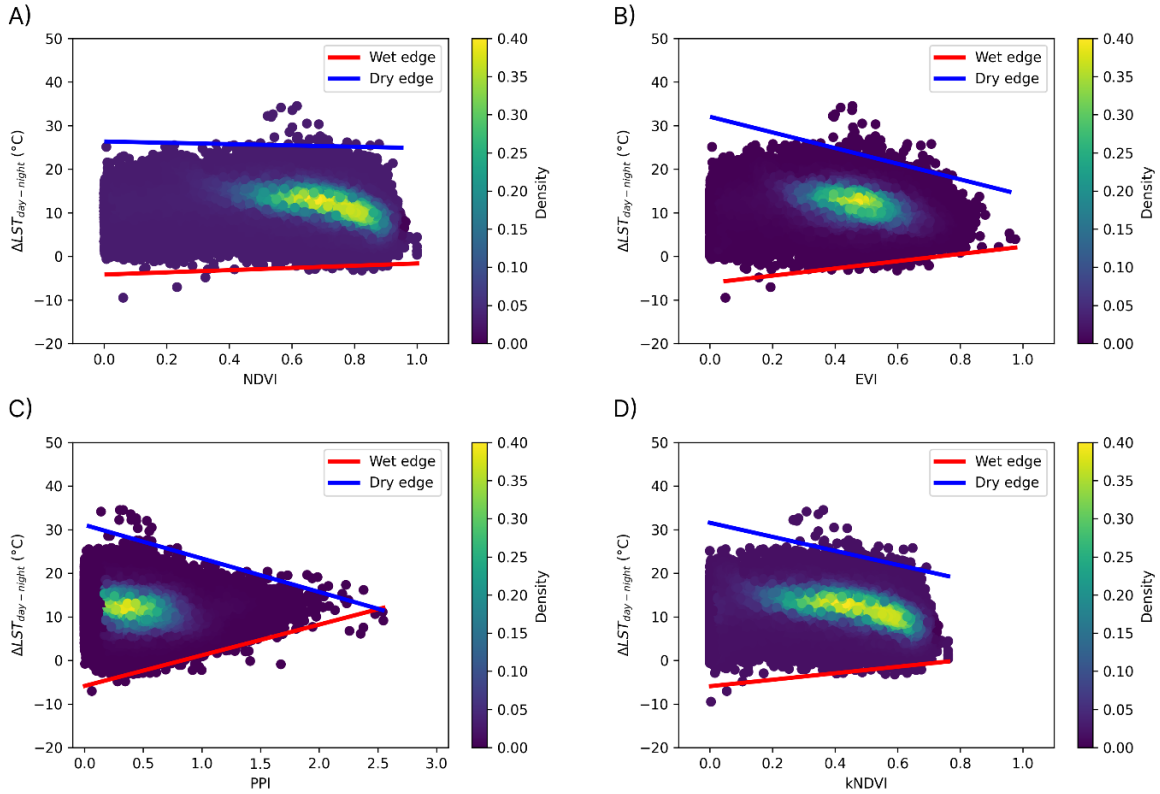

Figure 3. LST-VI triangular (trapezoidal) feature spaces for: A) Normalised Difference Vegetation Index (NDVI), B) Enhanced Vegetation Index (EVI), C) Plant Phenology Index (PPI) and D) kernel Normalised Difference Vegetation Index (kNDVI). For 2018 day #177 in study area 2.

A comparison of the LST-VI relationships of the different VIs showed that in the case of both wet and dry edges, NDVI had by far the most gradual slope, whilst non-saturated VIs such as EVI and kNDVI were considerably steeper. PPI had a slightly steeper slope than NDVI in both cases, but it also covered a larger range in values. With regards to the Y-intercept, values were more similar between the VIs, with the difference of the Y-intercepts for both wet edges and dry edges temperatures not exceeding 5°C. When comparing the variation of the slope parameters, NDVI showed the greatest temporal slope variance for the wet and dry edges. In the case of the dry edge, PPI had the second greatest temporal variability followed by EVI and then kNDVI with the lowest variability. In contrast for the wet edge slope, kNDVI had the most temporal variability following NDVI, whilst EVI and PPI had the lowest variance. The temporal variability of the Y-intercepts for all VIs and both edges are all very similar with the wet edges only having a difference of about 0.07 and dry edges only having a difference of about 0.03. A summarisation for the wet edge and dry edges can be seen on Tables 3 and 4 respectively.

Table 3. An overview of means and coefficients of variations (CV) of the wet edge slopes and Y-intercepts for the different VI in 2018 for study area 2.

Wet edge				
VI	**Slope (mean)**	**Y- Intercept (mean)**	**Slope (CV)**	**Y-Intercept (CV)**
EVI	19.60	-13.97	0.56	-0.83
NDVI	4.04	-10.94	1.45	-0.82
kNDVI	10.11	-12.69	0.84	-0.77
PPI	6.92	-10.79	0.57	-0.76

Table 4. An overview of means and CV of the dry edge slopes and Y-intercepts for the different VI in 2018 for study area 2.

Dry edge				
VI	**Slope (mean)**	**Y- Intercept (mean)**	**Slope (CV)**	**Y-Intercept (CV)**
EVI	-17.12	32.50	-0.37	0.15
NDVI	-4.95	28.75	-1.09	0.15
kNDVI	-19.47	33.55	-0.35	0.16
PPI	-6.49	29.53	-0.62	0.19

Looking at the same day for study area 1 in 2010, a similar pattern can be observed, with NDVI having near horizontal wet and dry edges and EVI and kNDVI have a more trapezoidal shape whilst PPI resembles more of a triangle, see Figure 4. In contrast to study area 2 however, the triangular feature space for NDVI, EVI and kNDVI are denser towards the lower end of the VI

spectrum while PPI with the broadest range fails to show any density hot spots. NDVI also seems to be lacking VI data in the lower end, causing the dry edge to flatten out and appear more horizontal, despite the point themselves showing a more trapezoidal shape.

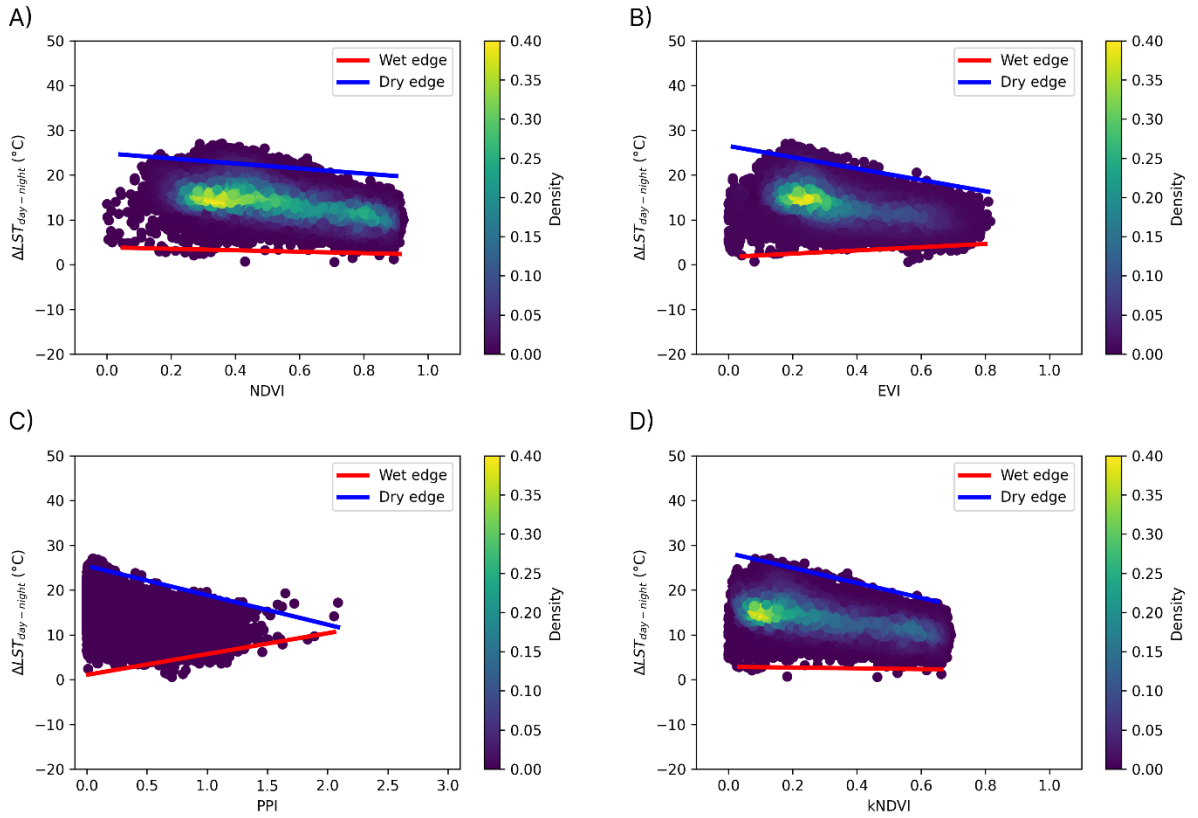

Figure 4. LST-VI triangular (trapezoidal) feature spaces for: A) NDVI, B) EVI, C) PPI and D) kNDVI. For 2010 day #177 in study area 1.

Calculating the mean slopes and intercept as well as the CV for the wet and dry edges in study area 1 for 2010 produced very similar results to study area 2, with PPI and NDVI showing the lowest mean slopes for both wet and dry edges whilst the Y-intercepts showed similar results for all the VIs. Furthermore, kNDVI and EVI showed the lowest variance for the dry edge slope, whilst kNDVI had higher variance for the wet edge slope whereas opposed to study area 2, NDVI produced a more stable slope. PPI produced the least amount of variance for the wet edge slope and the second highest variance for the dry edge slope after NDVI, the same ranking as for study area 2. A summarisation for the wet edge and dry edges can be seen on Tables 5 and 6 respectively.

Table 5. An overview of means and CV of the wet edge slopes and Y-intercepts for the different VI in 2010 for study area 1.

Wet edge				
VI	**Slope (mean)**	**Y- Intercept (mean)**	**Slope (CV)**	**Y-Intercept (CV)**
EVI	15.48	-8.31	0.80	-1.30
NDVI	3.55	-5.27	0.78	-1.88
kNDVI	9.75	-6.50	1.15	-1.67
PPI	5.03	9.08	0.58	-1.33

Table 6. An overview of means and CV of the dry edge slopes and Y-intercepts for the different VI in 2010 for study area 1.

Dry edge				
VI	**Slope (mean)**	**Y- Intercept (mean)**	**Slope (CV)**	**Y-Intercept (CV)**
EVI	-15.20	27.84	-0.26	0.13
NDVI	-5.54	25.28	-0.79	0.12
kNDVI	-19.89	29.92	-0.26	0.12
PPI	-8.36	27.45	-0.68	0.15

6.2 Spatial comparison

Looking closer at day #177 for 2018 corresponding to the earlier triangular feature spaces, a comparison of the resulting SM_d in addition to the original SM_{cr} and ΔLST are shown in Figure 5. All SM_d products were indistinguishable from one another, there seemed however to be a distintion on a more finer level, with $SM_{d\text{-}PPI}$ and $SM_{d\text{-}NDVI}$ having the lower max SM values. Whilst $SM_{d\text{-}kNDVI}$ had a significantly higher maximum values, correspond to an increase of around 0.14 m^3/m^3. Compared to the original SM_{cr}, the SM_d product showed very similar patterns when looking at the distribution of the maximum and minimum values, although the SM_d products seemed to overestimate the SM values and have a range of roughly double that of SM_{cr}, see Figure 5.

Similarly, looking at day #177 for 2010 in study area 1, Figure 6. The SM_d products are visually indistinguishably from one another. Dissimilarity to study area 2, however, SM_d products

seemed to have a significantly higher maximum SM value in study area 1, exceeding 1 m^3/m^3. This could be due to a pixel having a significantly higher VTCI value than the surrounding pixels bounded by the coarser resolution pixel. SMd-NDVI and SMd-EVI showed the highest SM values, whereas SMd-kNDVI and SMd-PPI showed more robustness to the effect of VTCI outliers having lower maximum SM values.

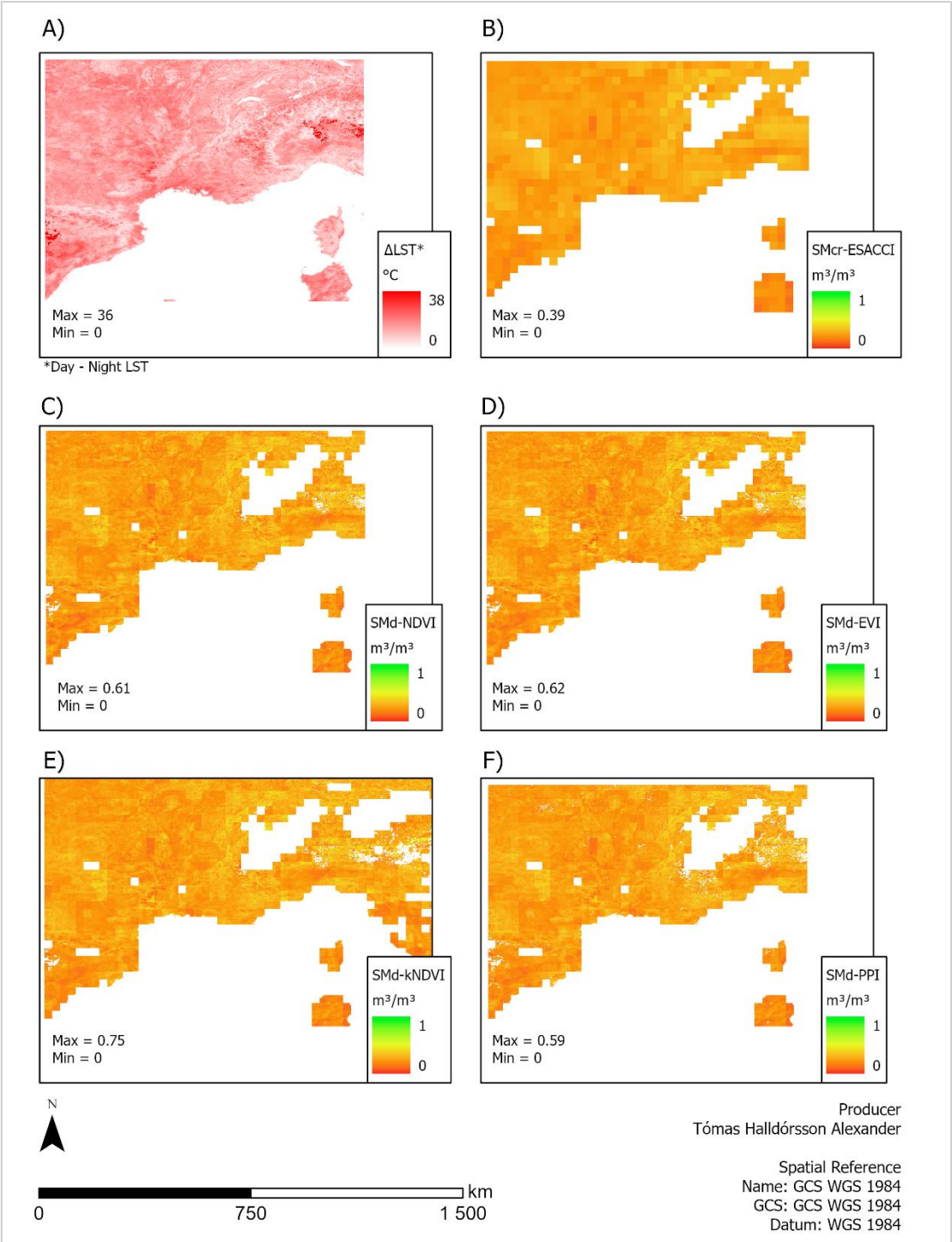

Figure 5. A visual comparison of: A) The difference in day and night temperatures (ΔLST), B) ESA CCI SM product ($SM_{cr\text{-}ESACCI}$), C) NDVI derived downscaled SM product ($SM_{d\text{-}NDVI}$), D) EVI derived downscaled product ($SM_{d\text{-}EVI}$), E) kNDVI derived downscaled product $SM_{d\text{-}kNDVI}$ and F) PPI derived downscaled product $SM_{d\text{-}PPI}$. For 2018 day #177 within study area 2.

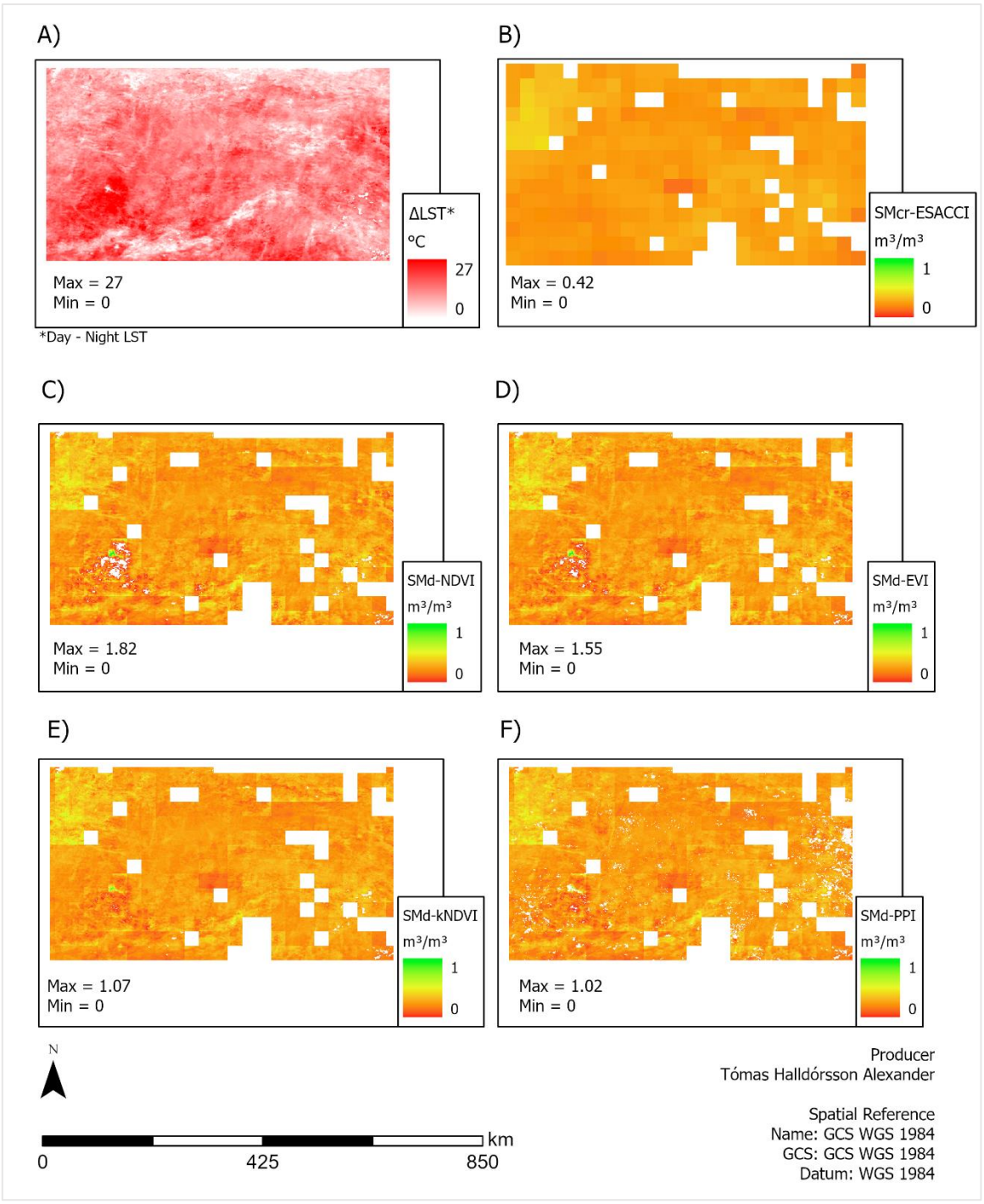

Figure 6. A visual comparison of: A) ΔLST, B) $SM_{cr\text{-}ESACCI}$ and the downscaled SM products: C) $SM_{d\text{-}NDVI}$, D) $SM_{d\text{-}EVI}$, E) $SM_{d\text{-}kNDVI}$ and F) $SM_{d\text{-}PPI}$. For 2010 day #177 within study area 1.

6.3 Evaluation with REMEDHUS ISMN network

The evaluation with the SM products against the in-situ measurements from the REMEDHUS ISMN network, showed that the original ESA CCI SM (SM_{cr}) product outperformed the SM_{d}

products in all sectors. Of the SM_d products, $SM_{d\text{-}kNDVI}$ performed best in terms of ubRMSD and *R* with a simple mean ubRMSD of 0.065 ± 0.035 m^3/m^3 and a simple and weighted mean *R* of 0.64 ± 0.15 and 0.71 respectively. $SM_{d\text{-}NDVI}$ showed the worst performance for all metrics, having a simple and weighted mean *R* values of 0.57 ± 0.15 and 0.63 respectively and mean ubRMSD value of 0.075 ± 0.032 m^3/m^3. An overview of the mean *R* and ubRMSD values are summarised in Table 7. Figures 7 and 8 show the boxplots for ubRMSD and *R* respectively. In terms of ubRMSD, all SM product showed consistent low ubRMSD values, with only a couple of outliers with high ubRMSD. In terms of *R*, the SM_d products showed more variation in their values but produced similar medians with only $SM_{cr\text{-}ESACCI}$ having a slightly higher median *R*.

Table 7. Simple and weighted mean correlations and ubRMSD for the different downscaled SM products and ESA CCI SM against the REMEDHUS network. Correlations and ubRMSD are also shown from a previous study by Peng et al. (2015) covering the same time period and study area.

Product	**R (Simple mean)**	**R (Weighted mean)**	**ubRMSD (m^3/m^3) (Simple mean)**
$SM_{d\text{-}NDVI}$	0.57 ± 0.15	0.63	0.075 ± 0.032
$SM_{d\text{-}PPI}$	0.62 ± 0.14	0.69	0.067 ± 0.035
$SM_{d\text{-}EVI}$	0.61 ± 0.14	0.67	0.069 ±0.033
$SM_{d\text{-}kNDVI}$	0.64 ± 0.15	0.71	0.065 ±0.035
$SM_{cr\text{-}ESACCI}$	0.70 ± 0.16	0.78	0.063 ± 0.036
$SM_{cr\text{-}ESACCI}$ Peng (2015)	0.53 ± 0.13	NA	0.05 ± 0.02
$SM_{d\text{-}LAI}$ Peng (2015)	0.42 ± 0.17	NA	0.06 ± 0.17

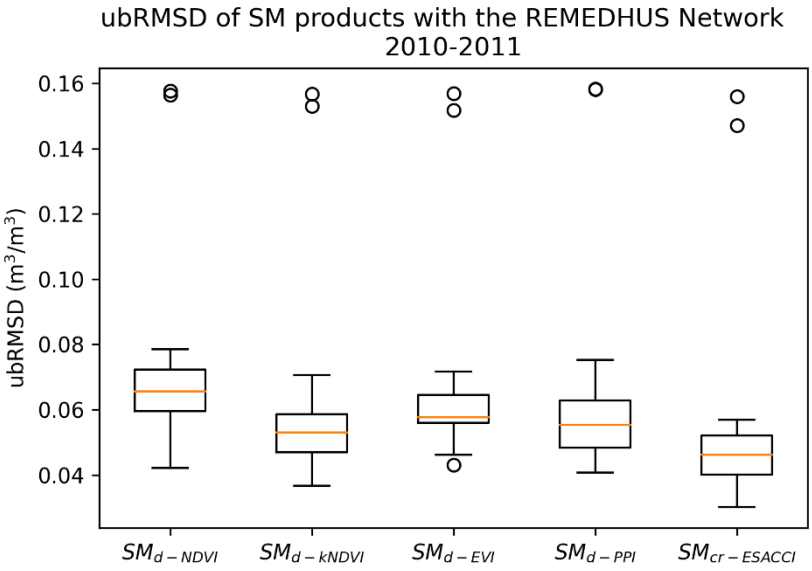

Figure 7. Boxplot for ubRMSD values for the different SM products with the REMEDHUS network.

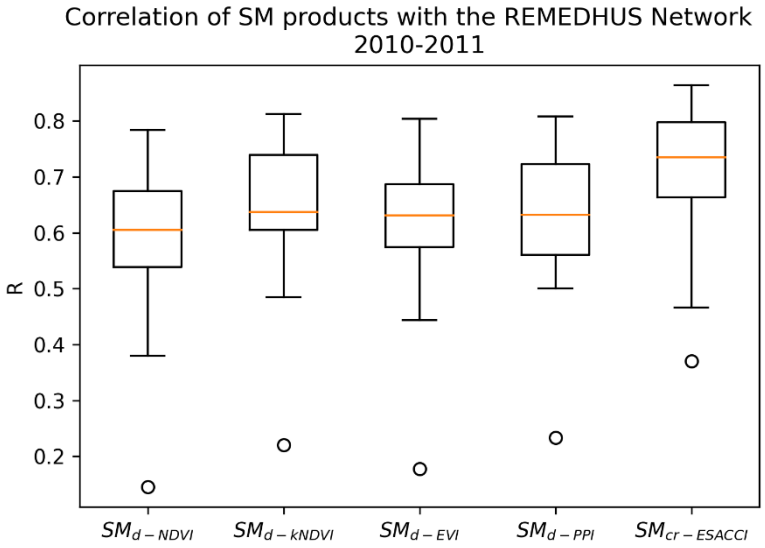

Figure 8. Boxplot for correlation coefficients (R) of the different SM products with the REMEDHUS network.

When comparing the individual stations, SM_{cr} had the highest *R* in 13 out of the 17 stations, only being outperformed by $SM_{d\text{-}PPI}$ at station I06, $SM_{d\text{-}kNDVI}$ at station N09 and $SM_{d\text{-}EVI}$ at station K10. Focusing on the SM_d products, $SM_{d\text{-}PPI}$ showed the highest *R* in 6 stations, $SM_{d\text{-}kNDVI}$ at 8 and $SM_{d\text{-}EVI}$ at 2 whilst $SM_{d\text{-}NDVI}$ never produced the best performance, see Figure 9 (A). Regarding ubRMSD, SM_{cr} had the best results in 15 stations, only being outperformed in N09 by $SM_{d\text{-}kNDVI}$. Out of the SM_d products, $SM_{d\text{-}kNDVI}$ had the best performance at 12 stations

each whilst $SM_{d\text{-}PPI}$ only outperformed in 3, $SM_{d\text{-}EVI}$ in one and $SM_{d\text{-}NDVI}$ in none, see Figure 9 (B).

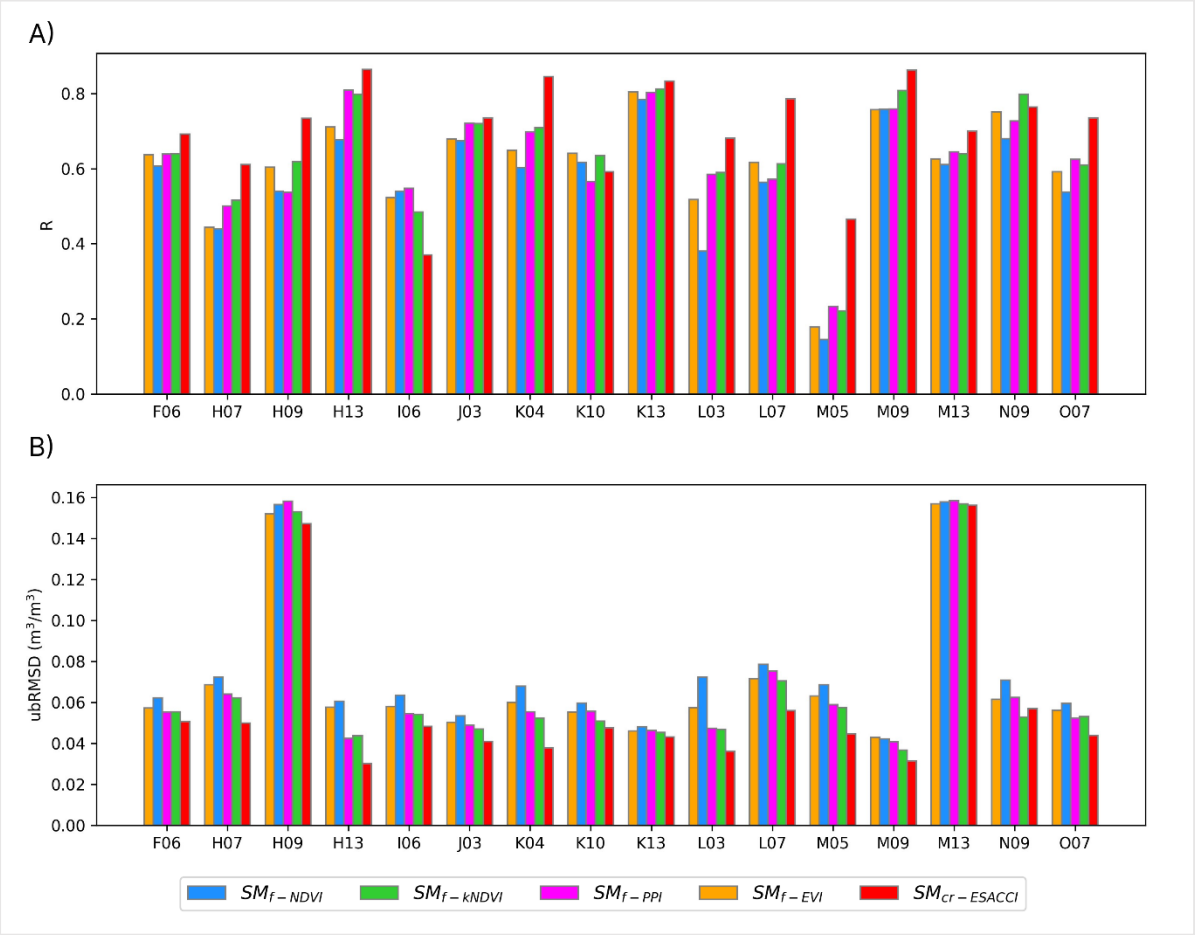

Figure 9. The evaluation metrics A) correlation coefficients (R), and B) ubRMSD of each SM product against the in-situ measurements for each station in the REMEDHUS network.

Stations M05 and K13 showed the worst and best correlations respectively. For station M05, $SM_{d\text{-}NDVI}$ had the lowest *R* of the SM_d products at 0.15, followed by $SM_{d\text{-}EVI}$ with 0.18, $SM_{d\text{-}kNDVI}$ with 0.22 and $SM_{d\text{-}PPI}$ at 0.24. The SM_{cr} product however had a much better correlation with an *R* of 0.47. Looking at Figure 10 (A) at the different SM plotted with the in-situ ground measurements it us shown that both the SM_d and SM_{cr} products overestimate SM relative to in-situ measurements, especially in the early parts 2010 where there seems to be no resemblance in the patterns. It can however be seen is that there was a clear similarity in temporal patterns and values between SM_d and SM_{cr}. For station K13, which showed the best correlation with the SM_d products, $SM_{d\text{-}kNDVI}$ has the highest *R* of 0.81, followed by $SM_{d\text{-}PPI}$ and $SM_{d\text{-}EVI}$ with 0.80 and $SM_{d\text{-}NDVI}$ at 0.78. Looking at Figure 10 (B) it is shown that the SM products matched the temporal pattern of the in-situ measurements and provide similar values.

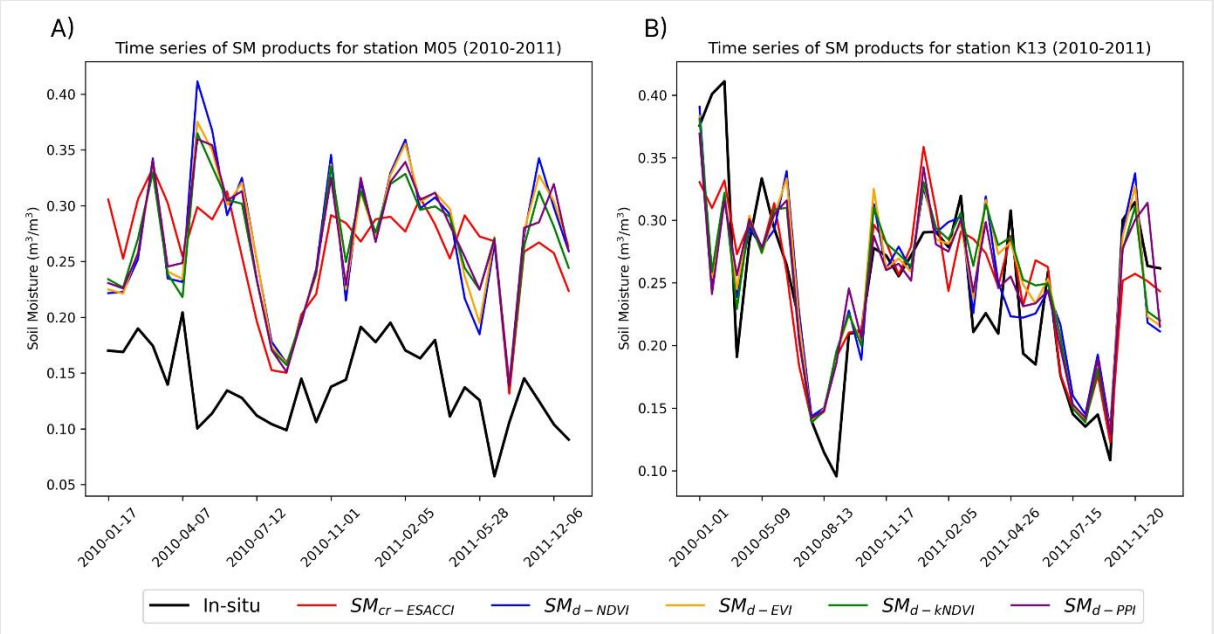

Figure 10. Time series of the SM products and in-situ measurements for: A) The worst correlated station (M05) and B) best correlated station (K13).

Stations M13 and M09 had the worst and best ubRMSD values respectively. For station M09, $SM_{d\text{-}EVI}$ has the worst ubRMSD of the SM_d products at 0.043 m^3/m^3, followed closely by $SM_{d\text{-}NDVI}$ at 0.042 m^3/m^3, $SM_{d\text{-}PPI}$ at 0.041 m^3/m^3 and $SM_{d\text{-}kNDVI}$ at 0.037 m^3/m^3. SM_{cr} had the lowest value at 0.031 m^3/m^3. Figure 11 (B) shows how the temporal patterns seem to match well with the in-situ measurements, but there also seems to be more noise for the SM_d products than the SM_{cr}. For station M13, all products showed very similar ubRMSD values, ranging from 0.156 m^3/m^3 for the SM_{cr} to 0.157 m^3/m^3 for both $SM_{d\text{-}kNDVI}$ and $SM_{d\text{-}EVI}$, whilst $SM_{d\text{-}PPI}$ and $SM_{d\text{-}NDVI}$ followed closely behind at 0.158 m^3/m^3. Looking at Figure 11 (A), big spikes can be shown for in-situ measurements in winter periods which are highly underestimated in the SM_{cr} and SM_d products, which can be explain the high ubRMSD.

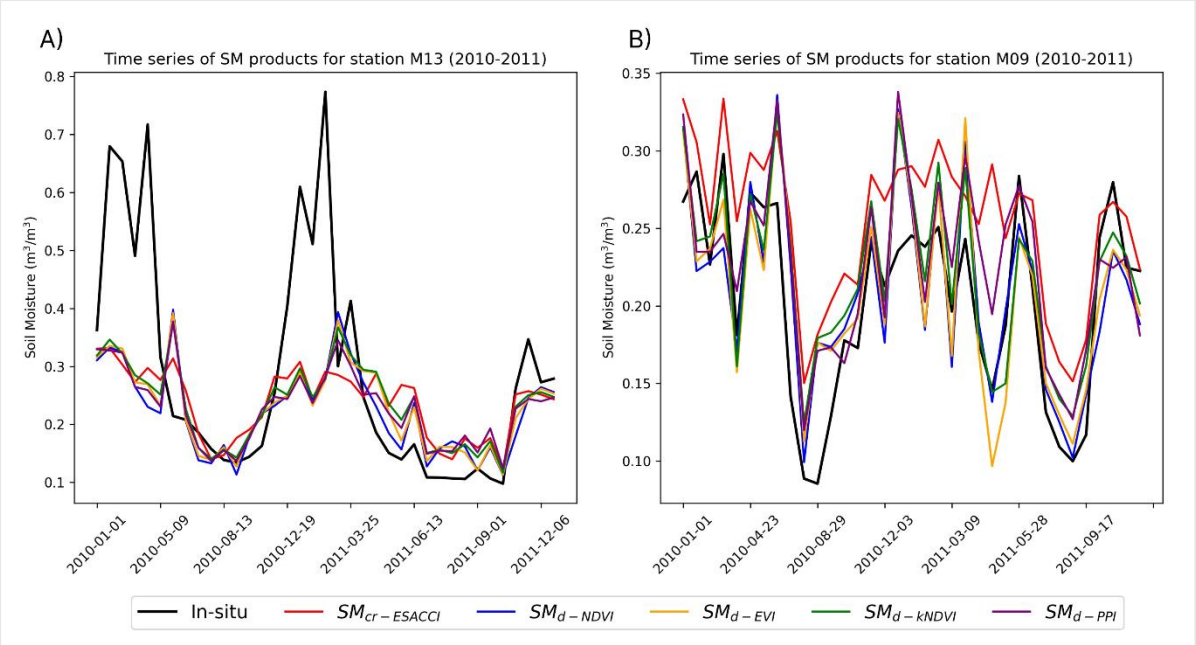

Figure 11. Time series of the SM products and in-situ measurements for: A) The station with the worst ubRMSD (M13) and B) The station with the best ubRMSD (M09).

6.4 Evaluation with SMOSMANIA ISMN network

In comparison to the evaluation with the REMEDHUS network, the SMOSMANIA stations in study area 2, showed similar results. The SM_{cr} product still outperformed the SM_d products, in all sectors. Of the SM_d products, all products produced similar ubRMSD, with $SM_{d\text{-}EVI}$ and $SM_{d\text{-}PPI}$ at 0.065 ± 0.014 m^3/m^3 and $SM_{d\text{-}kNDVI}$ at 0.059 ± 0.015 m^3/m^3 and $SM_{d\text{-}NDVI\ at}$ 0.060 ± 0.014 m^3/m^3. All SM_d products also produces similar correlations, $SM_{d\text{-}PPI}$ had a mean *R* of 0.61 ± 0.21, followed by $SM_{d\text{-}kNDVI}$ at 0.60 ± 0.21 and $SM_{d\text{-}PPI}$ and $SM_{d\text{-}NDVI}$ both at 0.60 ± 0.23. SM_{cr} had a greater *R* at 0.68 ± 0.17. On the other hand, comparing the weighted means, the SM_d products produced *R* more similarly to the SM_{cr} product with $SM_{d\text{-}EVI}$ and $SM_{d\text{-}PPI}$ at 0.75, $SM_{d\text{-}NDVI}$ at 0.74 and $SM_{d\text{-}kNDVI}$ at 0.73, whilst SM_{cr} only had a *R* of 0.76. An overview of the mean *R* and ubRMSD values are summarised in Table 8. Figures 12 and 13 show the boxplots for ubRMSD and *R* respectively. Compared to study area 1, the SM_d products showed less consistency in ubRMSD values but produced similar medians. $SM_{cr\text{-}ESACCI}$ had a lower median ubRMSD but produced more inconsistent results. However, in terms of *R*, $SM_{cr\text{-}ESACCI}$ showed more consistency than the SM_d products and produced a higher median *R*.

Table 8. Simple and weighted mean correlations and ubRMSD for the different downscaled SM products and ESA CCI SM against the SMOSMANIA network.

Product	R (Simple mean)	R (Weighted mean)	ubRMSD (m^3/m^3) (Simple mean)
$SM_{d\text{-}NDVI}$	0.60 ± 0.23	0.74	0.068 ± 0.014
$SM_{d\text{-}PPI}$	0.61 ± 0.21	0.75	0.065 ± 0.014
$SM_{d\text{-}EVI}$	0.60 ± 0.23	0.75	0.065 ± 0.014
$SM_{d\text{-}kNDVI}$	0.60 ± 0.21	0.73	0.067 ± 0.014
$SM_{cr\text{-}ESACCI}$	0.68 ± 0.17	0.76	0.055 ± 0.017

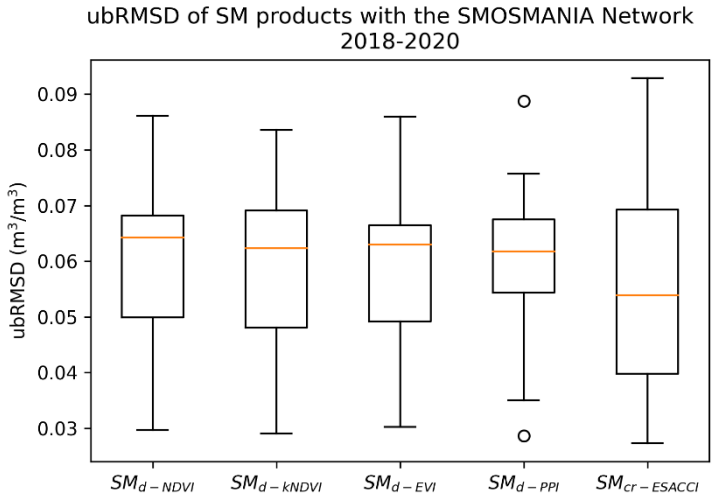

Figure 12. Boxplot for ubRMSD values for the different SM products with the SMOSMANIA network.

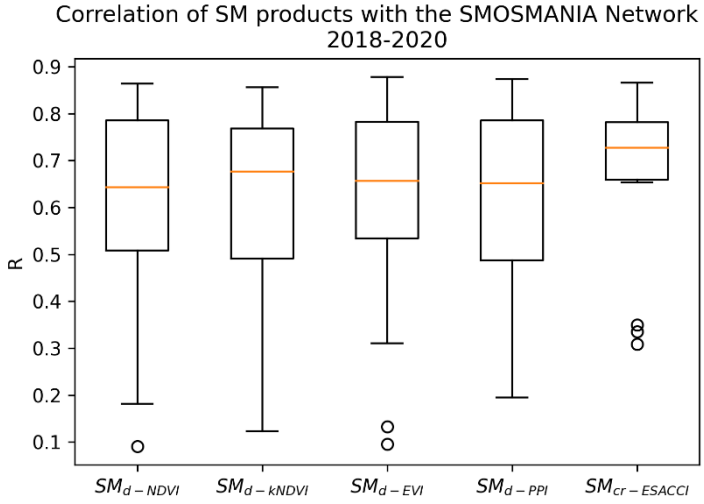

Figure 13. Boxplot for correlation coefficients (R) of the different SM products with the SMOSMANIA network.

When comparing the individual stations, the SM_{cr} had a higher *R* then SM_{d} products in most stations, having better correlation in 10 out of 18 stations, whilst $SM_{d\text{-}EVI}$ and $SM_{d\text{-}PPI}$ performed better in 4 stations each. Out of the SM_{d} products, $SM_{d\text{-}PPI}$ seemed to perform best, showing highest correlation at 7 stations, followed closely by $SM_{d\text{-}EVI}$, having best performance in 6 stations. $SM_{d\text{-}kNDVI}$ only showed the best performance in 4 station and $SM_{d\text{-}NDVI}$ in 1, Figure 14 (A). With regards to ubRMSD, SM_{cr} showed the best results in 11 out 18 stations, whilst $SM_{d\text{-}EVI}$ showed the best results in 3 stations and $SM_{d\text{-}PPI}$ in 1 station. Of the SM_{d} products, The $SM_{d\text{-}PPI}$ showed the best performance at 7 stations whilst $SM_{d\text{-}EVI}$ outperformed in 6, followed closely by $SM_{d\text{-}kNDVI}$ managing to outperform the other SM_{d} product in 4 stations. $SM_{d\text{-}NDVI}$ only managed to produce the best ubRMSD at 1 station, Figure 14 (B).

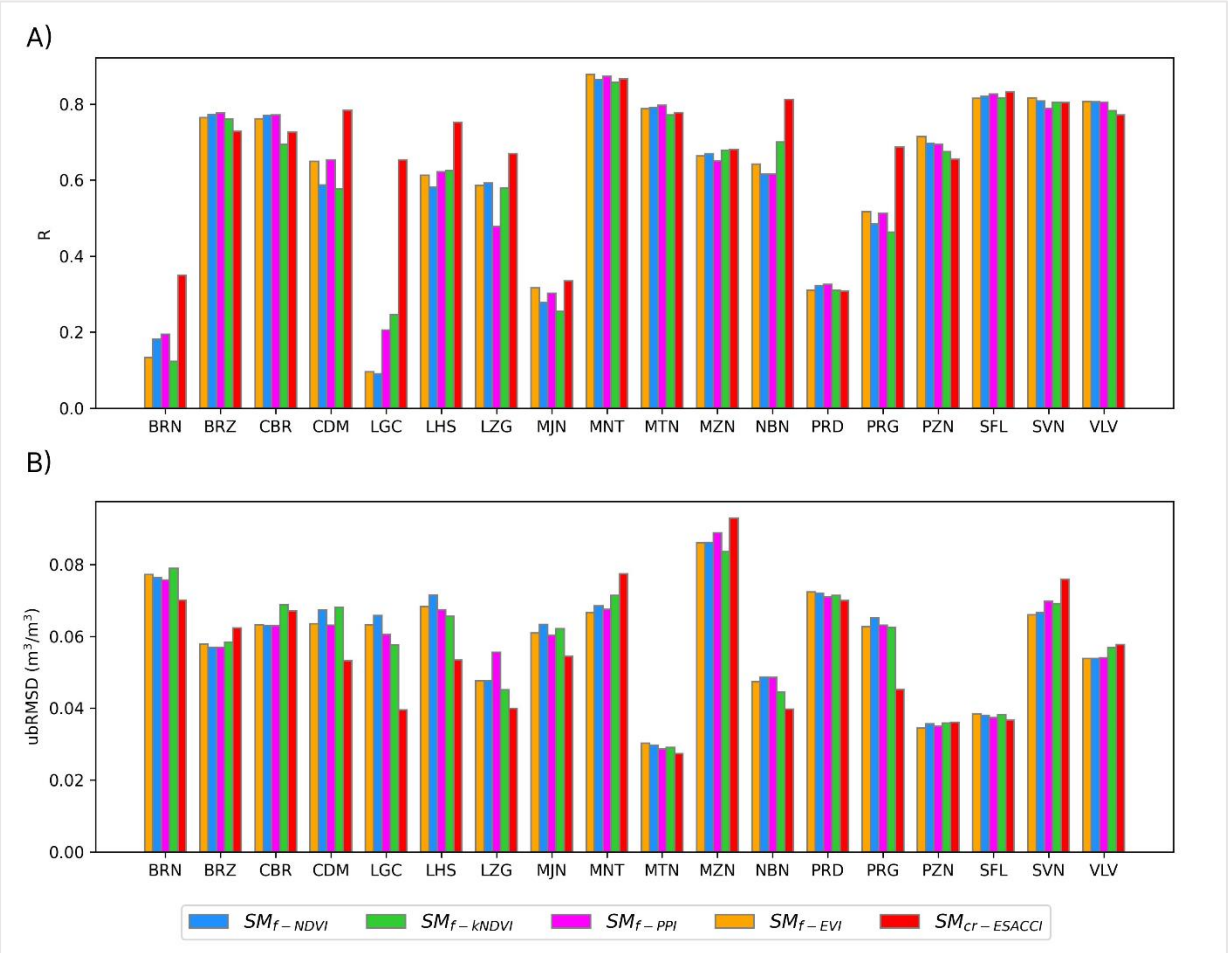

Figure 14. The evaluation metrics, A) correlation coefficient (R), and B) ubRMSD of each SM product against the in-situ measurements for each station in the SMOSMANIA network.

Stations LGC and MNT showed the worst and best correlations respectively. For station LGC, $SM_{d\text{-}NDVI}$ had the lowest *R* of the SM_{d} products at 0.09, followed by $SM_{d\text{-}EVI}$ at 0.10, $SM_{d\text{-}PPI}$ at

0.21 and $SM_{d\text{-}kNDVI}$ at 0.25. The SM_{cr} product however had a much better correlation with 0.65. Looking at Figure 15 (A) at the different SM plotted with the in-situ ground it is shown that the SM_d and SM_{cr} overestimate the SM everywhere, the SM_{cr} resembled the pattern of the in-situ measurements better whilst the SM_d products showed more sign of noise and extremes. For station MNT, which showed the best correlation with the downscaled products, $SM_{d\text{-}EVI}$ had the highest *R* of 0.88, followed by $SM_{d\text{-}PPI}$ at 0.87, and $SM_{d\text{-}NDVI}$ at 0.86 and $SM_{d\text{-}kNDVI}$ at 0.85. The SM_{cr} produced similar results, with a *R* of 0.87, only outperforming $SM_{d\text{-}kNDVI}$ and $SM_{d\text{-}NDVI}$. Looking at Figure 15 (B) it is shown that both the SM_d and SM_{cr} products matched the temporal pattern of the in-situ measurements very closely, but they did underestimate the in-situ SM significantly over the winter periods.

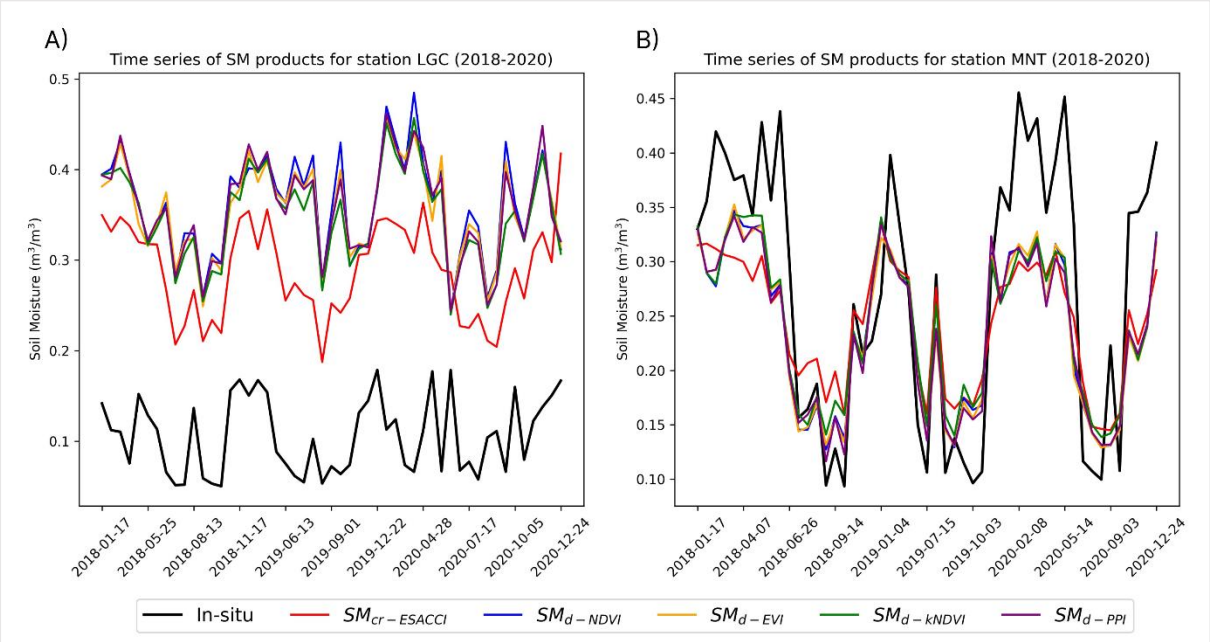

Figure 15. Time series of the SM products and in-situ measurements for: A) The worst correlated station (LGC) and B) the best correlated station (MNT).

Stations MZN and MTN had the worst and best ubRMSD values respectively. For station MZN, $SM_{d\text{-}PPI}$ had the highest ubRMSD of the SM_d products at 0.089 m^3/m^3, followed by $SM_{d\text{-}EVI}$ and $SM_{d\text{-}NDVI}$ with 0.086 m^3/m^3 and $SM_{d\text{-}kNDVI}$ at 0.084 m^3/m^3 with the best result. Overall SM_{cr} had the highest ubRMSD of 0.093 m^3/m^3, see Figure 16 (A). For station MTN, $SM_{d\text{-}EVI}$ and $SM_{d\text{-}NDVI}$ showed the highest ubRMSD at 0.03 m^3/m^3 of the SM_d products, followed very closely by $SM_{d\text{-}PPI}$ and $SM_{d\text{-}kNDVI}$ at 0.029 m^3/m^3. SM_{cr} produces the best ubRMSD at 0.027 m^3/m^3. Looking at Figure 16 (B) it is shown how the temporal patterns between the SM

products seem to show a temporal resemblance with slight overestimation of SM as compared to in-situ measurements.

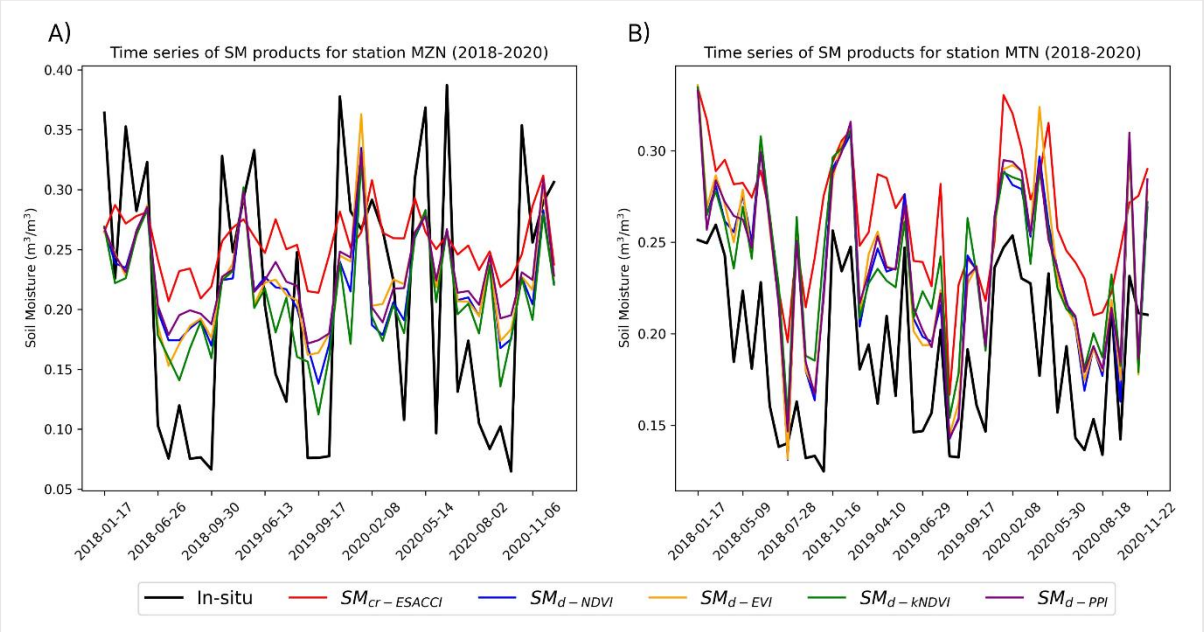

Figure 16. Time series of the SM products and in-situ measurements for: A) The station with the worst ubRMSD (MZN) and B) The station with the best ubRMSD (MTN).

7 Discussion

7.1 LST-VI relationships

Looking at the LST-VI relationships for study area 2 we can see how the different VI can have an influence on the results. In Figure 3, we can see how NDVI fails to show a trapezoidal or triangular relationship with the LST, having both wet and dry edges nearly horizontal resulting in a near constant VTCI value for all VI intervals which in turn will ignore any variety in the different landcovers and vegetation densities, thus creating a scaling factor solely dependent on the LST. For the same day, EVI, kNDVI and PPI produce a more trapezoidal or even a triangular relationship with LST, increasing the influence of the VI on the VTCI. A further investigation for the entire 2018 period, there can be seen a great difference in the mean slopes and their temporal variance whilst their Y-intercepts are more constant between the VI, see Figures 3 and 4. EVI seems to have the greatest mean slope for the wet edge whilst kNDVI has the greatest mean slope for the dry edge, indicating a greater heat increase with increasing VI. For both the wet and dry edges, NDVI has the most gradual mean slopes, followed by PPI. Although the range of PPI values is 3 times that of the other VI. Despite NDVI's failing to

show an adequate shape in the triangular feature space for the specific day, it does show the greatest variance in slope for both the dry edge and wet edge over the study period, indicating that its shape and therefore applicability can vary greatly throughout the time period. Compared to NDVI, EVI and kNDVI show the least amount of variance for both the dry and wet edge slopes, indicating more stable edges and less temporally variability. This contrast in variability of EVI and kNDVI as opposed to NDVI is likely a result of limited or absence of high valued VI pixels of EVI and kNDVI which can vary greatly through the year. Higher saturated VI values will lead to a more gradual slope and thus the shape of the NDVI triangular feature space will therefore be more sensitive by higher VI and subsequently have a greater temporal variability. kNDVI does however have a greater variance for the wet edge slope than EVI which could be as a result of EVI being better suited at ignoring canopy background signals and reduce atmospheric influences and thus potentially producing a more accurate product. This does however not explain why only the wet edge seems to be affected. PPI on the other hand, also avoiding saturation of dense vegetation, does not share EVI's and kNDVI's stable dry edge slope, having greater variance but being more stable than NDVI. Its wet edge slope is however more stable compared to the other VI, a contrasting relationship to kNDVI, whose dry edge is more stable than its wet edge.

7.2 Comparison with results of Peng et al (2015)

The result for study area 1 shows good results compared to evaluations performed by Peng et al. (2015) over the same period, using similar methods. In comparison with in-situ measurements, their downscaled SM product had a mean *R* of 0.42 ± 0.17, it is however not clarified whether this represents a simple or weighted mean. Nevertheless, assuming it is a simple mean, this study's SM_d provides a better result ranging from 0.57 ± 0.15 to 0.64 ± 0.15. In addition, it also shows a better *R* for SM_{cr} at 0.70 ± 0.16 as opposed to their mean *R* of 0.53 ± 0.13. In terms of ubRMSD, Peng et al (2015) results outperform results of this study with mean ubRMSD values of 0.06 ± 0.017 m^3/m^3 and 0.05 ± 0.02 m^3/m^3 for the SM_d and SM_{cr} respectively whereas this study shows mean ubRMSD values of 0.065 ± 0.035 m^3/m^3 to 0.075 ± 0.032 m^3/m^3 for the SM_d and 0.063 ± 0.036 m^3/m^3 for the SM_{cr}. Looking at the station individually, the constituency of this study and Peng et al. (2015) results vary, with stations such as H9 and M13 showing consistently high *R* and ubRMSD whilst other stations such J3 gives good correlation in this study as opposed a more lacking performance in Peng et al. (2015) study.

The varying results between the two studies could be influenced by the different methods in estimating the wet and dry edges between the two studies, whilst both studies used a best fitted linear line to determine the dry edges, Peng et al. (2015) used a fixed value for the wet edge, whilst this study used a dynamic wet edge, determined by a best fitted linear line, akin to the dry edge, thus resulting in more variance with changing VI value. Peng et al. (2015) also took more precautions in estimating the VTCI, by masking out high elevation areas to limit the influence of altitude on the temperature. In addition, Peng et al. (2015) limited themselves to only sampling homogenous landcover such as cropland. These precautions were not taken in this study, but nevertheless did manage to generally provide better results, indicating the limiting effect of these factors. This would however not explain the big difference in the SM_{cr} correlations between the two studies, which may be attributed to the sampling strategy. Dissimilarly to Peng et al (2015), this study negated three stations (E10, J14 and F11) from the evaluation due to their limiting data range resulting in smaller sampler sizes thus providing more unreliable correlation which will skew the overall results.

7.3 Evaluation with SMOSMANIA and REMEDHUS networks

The considerably larger study area, study area 2 shows very consistent results to study area 1 having only a slightly lower ubRMSD and higher standard deviation of the mean correlation for all the SM products. However, regarding the standard deviation, we would expect lower values in study area 2 as the temporal sample size is larger and we would expect the standard deviation to decrease with an increased sample size (Ramachandran & Tsokos, 2021). We do however also see the standard deviation being nearly the same for the SM_{cr} products for both study areas indicating that the standard deviation is less effected by the temporal sample size, but rather the downscaling method. This could be further explained by the increased variety in landcovers of the sample stations in study area 2, such as stations BRN, LGC and MJN which are all tree covered and show very poor correlations with the SM_{d} products. Indicating the inconsistency and insufficiency of using methods described in this study with different landcovers. That being said, in contrast to the correlation, the ubRMSD values are better in study area 2, having both a lower mean and standard deviation of ubRMSD which might be due to the high ubRMSD for stations H9 and M13 in study area 1 and the fewer stations used in said network.

7.4 Comparison of the downscaled soil moisture products

Comparing the performance of the different VIs for both study areas, all VIs show promising results, not deviating more than a tenth in *R* and a hundredth in ubRMSD from one another and producing overlapping performance with respect to standard deviations. However, looking closer at the individual stations, we see a different picture. For study area 2, $SM_{d\text{-}EVI}$ and $SM_{d\text{-}PPI}$ give the most consistently good results, both having the very similar *R* and ubRMSD for all stations. We do see that $SM_{d\text{-}EVI}$ generally outperforms the $SM_{d\text{-}PPI}$ at stations in vineyards such as PZN, non-irrigated arable lands such as PRG, SVN and quite significantly in the urban areas such as LZG. $SM_{d\text{-}PPI}$ manages to give better results for forested, higher vegetation areas, such as stations LGC and BRN where despite not showing a significant correlation still produced results notably better than EVI.

For study area 1, there are no tree covered stations, thus a comparison between the areas is lacking for the forested areas, there are however non-irrigated arable lands and vineyards. In contrast to study area 2, for the study area 1, $SM_{d\text{-}PPI}$ seems to outperform $SM_{d\text{-}EVI}$ significantly in most stations, including stations in non-irrigated arable lands and vineyards. Alternatively, $SM_{d\text{-}kNDVI}$ shows good consistently good results, outperforming the other SM_d products at 8 stations in terms of *R* and 12 stations in terms of ubRMSD. But similarly, to $SM_{d\text{-}EVI}$, its performance slightly drops between study areas. In study area 1, $SM_{d\text{-}kNDVI}$ struggles to keep up with $SM_{d\text{-}NDVI}$ and is outperformed by it in terms of *R* in 14 of 18 stations, 2 of which happened to be forested regions. Indicating the potential of using $SM_{d\text{-}kNDVI}$ in densely vegetated areas and its limits in sparser vegetation. This cannot however be claimed to be true for both study area, as there seems to be shift in performance for $SM_{d\text{-}kNDVI}$ between the stations. The inconsistency in $SM_{d\text{-}kNDVI}$ performance could be explained by the heuristic approach in Equation 9, assuming σ represent the average values of Red and NIR bands. Whilst for optimum performance a specific σ values should be chosen for different areas, as higher σ values are more sensitive to denser vegetation and lower σ values are more sensitive to sparser vegetation. The heuristic, although simple could thus lead to poor results, specifically in the plotting of the triangular features space as the index will only being optimised for low or high VI values which in turn greatly affect the wet and dry edges. Thus, this generalisation may not be suitable for larger areas with a lot of variety vegetation and landcovers. Further evaluation must however be conducted to state such a claim. What this study's results do show is that $SM_{d\text{-}PPI}$, although not always having the best results, does show consistency between the two

study areas which $SM_{d\text{-}kNDVI}$ and $SM_{d\text{-}EVI}$ fail to do. But also, that PPI manages to keep up with the other VIs, and in some cases outperforms them, in an environment in which its not developed to thrive or have an advantage further showing its potential to thrive in areas where it does have an advantage, such as the northern latitudes and forested areas. The reason for its good performance could be due to its sensitivity to the soil differential index (DVI) and LAI, see Equation 8, two factors which have been shown to be closely related to soil (Jin & Eklundh, 2014; Peng et al., 2015). It should however be noted that the PPI data had a temporal resolution of 1 day as opposed to the other VIs with 16-day resolution, this could have affected the overall result as daily data was compared with composite data. Nevertheless, as PPI is considered more sensitive to noise than other VI, we could expect correlations to increase by compositing PPI and thus decreasing the noise. If we assume the PPI value does not fluctuate significantly within the compositing period (Jin & Eklundh, 2014).

7.5 Limitations of this study

Throughout this study, many limitations were met, mainly in the form of data availability and quality. For instance, the VI products limit the temporal resolutions to 16-day intervals which greatly reduces the sample size to only 23 images a year, thus increasing the margin of error. Furthermore, the VI values do not represent the surface of the specific day as this study uses composites for the VIs based on the quality of the pixel over an 8-day period. This is however a limitation which has been met in a variety of studies using the same data and does not solely effect this study (Kim & Hogue, 2012; Peng et al., 2016). The LST suffers the same issues as 8-day averages are used and it is assumed that the temperature does not vary greatly within the 8-day period. Kim and Hogue (2012) met the same limitations using averaged LST but compared there results with daily LST temperatures and found that daily LST produced generally better correlations. However, by using the daily LST they met other limitations with cloud cover significantly effecting their data availability. Using a downscaling factor also has its limits, as it is a more general approach which lacks consideration of variations in terrain and atmospheric background and is less dependent on physical processes. Furthermore, they are highly dependent on the accuracy of the satellite data and the fitting of the triangular feature space, which may cause uncertainties if not adjusted in a suitable manner (Zhao et al., 2022). However, despite these limits, the downscaling of SM with a scaling factor has still managed to produce satisfactory results in a variety of studies across different regions ((Kim & Hogue, 2012; Peng et al., 2015, 2016)). Other issues arose when looking for a study area due to the

limiting amount of SM networks, in suitable locations with good hydrological contrasts, constituent data availability, quantity of stations and relevant measurements. Even with a suitable amount of sample stations, such as in this study, there are still issues regarding their positions, for example the SMOSMANIA network covers a variety of different landcovers but there are too few stations for each landcover to provide a proper evaluation between them, similar limitation have been met in a variety of studies, due to the lack of ground measurements able to represent the otherwise complex landscape (Liu et al., 2021). Another limitation includes the choice of methods used in this study, as there are many different alterations and ways which have been used to downscale SM with optical and thermal based methods which were not evaluated in this study due to time constraints and overall scope of the study (Garcia et al., 2014; Kim & Hogue, 2012; Peng & Loew, 2017).

7.6 Recommendations for future studies

This study opens a wide range of questions which can further motivate future studies. More generally, it would be interesting to look at the other downscaling methods and alterations, such as using a fixed wet edge, or using quantiles to determine the extremum temperatures with the different VIs. It would also be interesting to look at the effects of the size of study area on the downscaling process, a repeated study could be done for study area 2, using a smaller study area around the SMOSMANIA network and compare the results. Additionally, due to the similar performance of the mean metrics and overlapping results a further, more thorough evaluation should be conducted using more advanced statistical test such as a significance analysis. This study shows the possibilities of using different VI and further studies can be done to discover their fullest potential. kNDVI could be further enhanced using a more optimised σ value and proper testing should be conducted to fully evaluate its effect on the downscaling process. Furthermore, PPI's fullest potential should be investigated in areas of higher latitudes and denser vegetation, such as the FMI network in Finland to see how it compares with other VI in areas where it is advantageous.

8 Conclusions

This study aimed at evaluating and comparing the influence of using four different vegetation indexes VIs on spatial downscaling of ESA CCI soil moisture (SM) product at the coarse spatial resolution with the Vegetation Temperature Condition Index (VTCI) based method. Four considered VIs include NDVI, EVI, the kernel NDVI (kNDVI) and Plant Phenology Index

(PPI). The downscaled SM estimates were evaluated in two study areas, study area 1 surrounding the REMEDHUS network in northern Spain and study area 2 surrounding the SMOSMANIA network in southern France. The results showed that in terms of evaluation metrics, such as ubRMSD and *R*, the different VIs seem to influence the overall accuracy of the product. All VIs produced very similar results with mean *R* not deviating by more than 0.07 and 0.01 for study areas 1 and 2 respectively and mean ubRMSD not deviating by more than 0.01 and 0.001 for study areas 1 and 2 respectively. Comparing the temporal and spatial patterns visually of the different downscaled SM products did not show any distinguishable difference, as the downscaled SM products seemed to follow each other closely in a time series and produce similar results spatially. However, more significant results could be seen on a per station basis where PPI outperformed in most stations in terms of *R*, whereas kNDVI performed the best in most stations in terms of ubRMSD. EVI showed lacking performance compared to the kNDVI and PPI but did show improved results over NDVI which only produced best *R* at 1 station.

Regarding the performance of the downscaled SM products in different regions, the consistency seemed to be dependent on the VI. Whereas PPI and NDVI produced consistent results for both study areas, the performance of the EVI and kNDVI derived SM seemed to be more dependent on the study area. For study area 1, kNDVI produced great results, having the highest mean *R* of 0.64 ± 0.15 and the lowest ubRMSD of 0.065 ± 0.035 m^3/m^3 and outperforming the other downscaled SM products in 8/17 and 12/18 stations for *R* and ubRMSD respectively. However, in study are 2, kNDVI produces comparatively worse results, only outperforming the other downscaled SM products in 4/18 stations for both *R* and ubRMSD. EVI showed good performance in study area 2, outperforming the other SM_d products in 6/18 and 5/18 stations for *R* and ubRMSD respectively. The performance of EVI is however lacking in study area 1 where it has the second lowest mean *R* of 0.61 ± 0.14 and second highest ubRMSD of 0.069 ± 0.033 m^3/m^3 and only outperforms the other downscaled SM products in 1/16 and 2/16 stations for ubRMSD and *R* respectively.

In comparison to the original coarse SM product, the downscaled SM products generally did not yield improved results. The original ESA CCI SM product had much better performance in terms of higher *R* and lower ubRMSD, with a mean *R* of 0.70 ± 0.16 for study area 1 and 0.68 ± 0.17 for study area and a ubRMSD of 0.063 ± 0.036 m^3/m^3 and 0.055 ± 0.017 m^3/m^3 for study area 1 and 2, respectively. For study area 1, the downscaled SM products only managed

to outperform the coarser SM product in terms of *R* in 3 out of 16 stations. For study area 2, they only managed to outperform the coarse SM product in terms of *R* in 8 out of 18 stations. Results showed that the accuracy of the coarse SM product is not conserved in the downscaling process and generally outperforms the downscaled SM products in near all cases for both ubRMSD and *R* in both study areas.

This study encountered several limitations. First, the temporal resolution of the data used, such as the 8-day averaged LST and 16-day VIs may not capture the full dynamics of the variables, which affects the accuracy of the spatial downscaling method. Secondly, various alterations and alternative approaches for downscaling SM with VTCI-based methods were not evaluated in this study due to time constraints and overall scope of the study. Thirdly, the limited number of stations covering a wide range of land covers also restricted the practicality of conducting a comprehensive land cover-based evaluation. Although these factors acted as limitations in this study, they do serve as motivation for further research. Further studies could compare and evaluate the effects of using mean and daily LST data, to further understand its influence on the spatial downscaling results. It is also important to test the VIs with the different alterations of the VTCI based method, for example using a fixed wet edge or quantiles to determine the upper and lower limits of the edges. Furthermore, studies and evaluations should be conducted for the different VIs in different climates and regions, especially PPI which has produced consistent good results in low latitude regions with sparse vegetation where it has no significant advantage over the other VIs, as opposed to if it were evaluated in northern regions with dense vegetation and snow cover.

References

Attema, E. P. W. (1991). The Active Microwave Instrument on-board the ERS-1 satellite. *Proceedings of the IEEE*, *79*(6), 791–799. https://doi.org/10.1109/5.90158

Camps-Valls, G., Campos-Taberner, M., Moreno-Martínez, Á., Walther, S., Duveiller, G., Cescatti, A., Mahecha, M. D., Muñoz-Marí, J., García-Haro, F. J., Guanter, L., Jung, M., Gamon, J. A., Reichstein, M., & Running, S. W. (2021). A unified vegetation index for quantifying the terrestrial biosphere. *Science Advances*, *7*(9), eabc7447. https://doi.org/10.1126/sciadv.abc7447

Chifflard, P., Kranl, J., Strassen, G., & Zepp, H. (2018). The significance of soil moisture in forecasting characteristics of flood events. A statistical analysis in two nested catchments. *Journal of Hydrology and Hydromechanics*, *66*, 1–11. https://doi.org/10.1515/johh-2017-0037

Chuvieco, E. (2016). Spectral Vegetation Indices. In *Fundamentals of Satellite Remote Sensing, An Environmental Approach, Second Edition*. CRC Press.

Civeira, G. (2019). Introductory Chapter. In *Soil Moisture*. IntechOpen. https://doi.org/10.5772/intechopen.83603

Das, K., & Paul, P. K. (2015). Present status of soil moisture estimation by microwave remote sensing. *Cogent Geoscience*, *1*(1), 1084669. https://doi.org/10.1080/23312041.2015.1084669

Dorigo, W., Wagner, W., Albergel, C., Albrecht, F., Balsamo, G., Brocca, L., Chung, D., Ertl, M., Forkel, M., Gruber, A., Haas, E., Hamer, P., Hirschi, M., Ikonen, J., Jeu, R., Kidd, R., Lahoz, W., Liu, Y. Y., Miralles, D., & Lecomte, P. (2017). ESA CCI Soil Moisture for improved Earth system understanding: State-of-the art and future directions. *Remote Sensing of Environment*, *203*. https://doi.org/10.1016/j.rse.2017.07.001

Entekhabi, D., Reichle, R. H., Koster, R. D., & Crow, W. T. (2010). Performance Metrics for Soil Moisture Retrievals and Application Requirements. *Journal of Hydrometeorology*, *11*(3), 832–840. https://doi.org/10.1175/2010JHM1223.1

Entekhabi, D., Yueh, S., O'neill, P., Kellogg, K., Allen, A., Bindlish, R., Brown, M. E., Chan, S., Colliander, A., Crow, W., Das, N., Lannoy, G., Dunbar, R., Edelstein, W., Entin, J., Escobar, V., Goodman, S., Jackson, T., Jai, B., … West, R. (2014). *SMAP Handbook–Soil Moisture Active Passive: Mapping Soil Moisture and Freeze/Thaw from Space*. https://www.semanticscholar.org/paper/SMAP-Handbook%E2%80%93Soil-Moisture-Active-Passive%3A-Mapping-Entekhabi-Yueh/8ba9c2e6277b1960c36192f68dd50e0041054fe8

ESA. (n.d.). *ERS Overview*. Earth Online. Retrieved 8 May 2023, from https://earth.esa.int/eogateway/missions/ers/description

EUMETSAT. (2020a, April 15). *Metop series*. EUMETSAT. https://www.eumetsat.int/our-satellites/metop-series

EUMETSAT. (2020b, May 5). *Advanced SCATterometer (ASCAT)*. EUMETSAT. https://www.eumetsat.int/ascat

Fathololoumi, S., Vaezi, A. R., Firozjaei, M. K., & Biswas, A. (2021). Quantifying the effect of surface heterogeneity on soil moisture across regions and surface characteristic. *Journal of Hydrology*, *596*, 126132. https://doi.org/10.1016/j.jhydrol.2021.126132

Fensholt, R., Sandholt, I., & Stisen, S. (2006). Evaluating MODIS, MERIS, and VEGETATION vegetation indices using in situ measurements in a semiarid environment. *IEEE Transactions on Geoscience and Remote Sensing*, *44*(7), 1774–1786. https://doi.org/10.1109/TGRS.2006.875940

Gałęzewski, L., Jaskulska, I., Jaskulski, D., Lewandowski, A., Szypłowska, A., Wilczek, A., & Szczepańczyk, M. (2021). Analysis of the need for soil moisture, salinity and temperature sensing in agriculture: A case study in Poland. *Scientific Reports*, *11*. https://doi.org/10.1038/s41598-021-96182-1

Garcia, M., Fernández, N., Villagarcía, L., Domingo, F., Puigdefábregas, J., & Sandholt, I. (2014). Accuracy of the Temperature–Vegetation Dryness Index using MODIS under water-limited vs. Energy-limited evapotranspiration conditions. *Remote Sensing of Environment*, *149*, 100–117. https://doi.org/10.1016/j.rse.2014.04.002

Gruber, A., Su, C.-H., Crow, W. T., Zwieback, S., Dorigo, W. A., & Wagner, W. (2016). Estimating error cross-correlations in soil moisture data sets using extended collocation analysis. *Journal of Geophysical Research: Atmospheres*, *121*(3), 1208–1219. https://doi.org/10.1002/2015JD024027

Guha, A., & Lakshmi, V. (2004). Use of the scanning multichannel microwave radiometer (SMMR) to retrieve soil moisture and surface temperature over the central United States. *IEEE Transactions on Geoscience and Remote Sensing*, *42*(7), 1482–1494. https://doi.org/10.1109/TGRS.2004.828193

Huete, A., Didan, K., Miura, T., Rodriguez, E. P., Gao, X., & Ferreira, L. G. (2002). Overview of the radiometric and biophysical performance of the MODIS vegetation indices. *Remote Sensing of Environment*, *83*(1), 195–213. https://doi.org/10.1016/S0034-4257(02)00096-2

Jackson, T. J., Bindlish, R., Cosh, M., & Zhao, T. (2012). SMOS soil moisture validation with dense networks: Preliminary results. In C. M. U. Neale & M. H. Cosh (Eds.), *Remote Sensing and Hydrology* (Vol. 352, pp. 21–24). Int Assoc Hydrological Sciences. https://www.webofscience.com/wos/woscc/full-record/WOS:000313596500005

Jiang, Z., Huete, A. R., Didan, K., & Miura, T. (2008). Development of a two-band enhanced vegetation index without a blue band. *Remote Sensing of Environment*, *112*(10), 3833–3845. https://doi.org/10.1016/j.rse.2008.06.006

Jin, H., & Eklundh, L. (2014). A physically based vegetation index for improved monitoring of plant phenology. *Remote Sensing of Environment*, *152*, 512–525. https://doi.org/10.1016/j.rse.2014.07.010

Kim, J., & Hogue, T. S. (2012). Improving Spatial Soil Moisture Representation Through Integration of AMSR-E and MODIS Products. *IEEE Transactions on Geoscience and Remote Sensing*, *50*(2), 446–460. https://doi.org/10.1109/TGRS.2011.2161318

Liu, Y., Zhu, Q., Liao, K., Lai, X., & Wang, J. (2021). Downscaling of ESA CCI soil moisture in Taihu Lake Basin: Are wetness conditions and non-linearity important?

Journal of Water and Climate Change, *12*(5), Article 5. https://doi.org/10.2166/wcc.2020.131

Mao, T., Shangguan, W., Li, Q., Li, L., Zhang, Y., Huang, F., Li, J., Liu, W., & Zhang, R. (2022). A Spatial Downscaling Method for Remote Sensing Soil Moisture Based on Random Forest Considering Soil Moisture Memory and Mass Conservation. *Remote Sensing*, *14*(16), Article 16. https://doi.org/10.3390/rs14163858

Merlin, O., Walker, J. P., Chehbouni, A., & Kerr, Y. (2008). Towards deterministic downscaling of SMOS soil moisture using MODIS derived soil evaporative efficiency. *Remote Sensing of Environment*, *112*(10), 3935–3946. https://doi.org/10.1016/j.rse.2008.06.012

Minnett, P. J. (2019). Satellite Remote Sensing of Sea Surface Temperatures☆. In J. K. Cochran, H. J. Bokuniewicz, & P. L. Yager (Eds.), *Encyclopedia of Ocean Sciences (Third Edition)* (pp. 415–428). Academic Press. https://doi.org/10.1016/B978-0-12-409548-9.04340-2

Mousa, B. G., & Shu, H. (2020). *Spatial Evaluation and Assimilation of SMAP, SMOS, and ASCAT Satellite Soil Moisture Products Over Africa Using Statistical Techniques*. *7*(1). https://doi.org/10.1029/2019EA000841

NASA. (n.d.). *TRMM Microwave Imager (TMI)*. Global Precipitation Measurement. Retrieved 8 May 2023, from https://gpm.nasa.gov/missions/TRMM/satellite/TMI

NASA. (2020, April 10). *What is Synthetic Aperture Radar?* [Backgrounder]. Earthdata; Earth Science Data Systems, NASA. https://www.earthdata.nasa.gov/learn/backgrounders/what-is-sar

National Satellite Meteorological Center. (n.d.). *FY-3B*. National Satellite Meteorological Center. Retrieved 8 May 2023, from https://www.nsmc.org.cn/nsmc/en/satellite/FY3B.html

National Snow and Ice Data center. (n.d.). *SMMR, SSM/I, and SSMIS Sensors Summary*. NSIDC. https://nsidc.org/sites/default/files/smmr-ssmi-ssmis-sensors_0.pdf

NIDIS. (n.d.). *Soil Moisture*. Drought.Gov. Retrieved 19 May 2023, from https://www.drought.gov/topics/soil-moisture

OSCAR. (n.d.). *WMO OSCAR | Details for Instrument MWRI-1*. Observing Systems Capability Analysis and Review Tool. Retrieved 8 May 2023, from https://space.oscar.wmo.int/instruments/view/mwri_1

Parrens, M., Wigneron, J.-P., Richaume, P., Mialon, A., Al Bitar, A., Fernandez-Moran, R., Al-Yaari, A., & Kerr, Y. H. (2016). Global-scale surface roughness effects at L-band as estimated from SMOS observations. *Remote Sensing of Environment*, *181*, 122–136. https://doi.org/10.1016/j.rse.2016.04.006

Peng, J., Albergel, C., Balenzano, A., Brocca, L., Cartus, O., Cosh, M. H., Crow, W. T., Dabrowska-Zielinska, K., Dadson, S., Davidson, M. W. J., de Rosnay, P., Dorigo, W., Gruber, A., Hagemann, S., Hirschi, M., Kerr, Y. H., Lovergine, F., Mahecha, M. D., Marzahn, P., … Loew, A. (2021). A roadmap for high-resolution satellite soil moisture applications – confronting product characteristics with user requirements. *Remote Sensing of Environment*, *252*, 112162. https://doi.org/10.1016/j.rse.2020.112162

Peng, J., Alexander, L., Merlin, O., & Verhoest, N. E. C. (2017). *A review of spatial downscaling of satellite remotely sensed soil moisture*. *55*(2), 341–366. https://doi.org/10.1002/2016RG000543

Peng, J., & Loew, A. (2017). Soil moisture downscaling using a simple thermal based proxy. *2017 IEEE International Geoscience and Remote Sensing Symposium (IGARSS)*, 2503–2506. https://doi.org/10.1109/IGARSS.2017.8127503

Peng, J., Loew, A., Zhang, S., Wang, J., & Niesel, J. (2016). Spatial Downscaling of Satellite Soil Moisture Data Using a Vegetation Temperature Condition Index. *IEEE Transactions on Geoscience and Remote Sensing*, *54*(1), 558–566. https://doi.org/10.1109/TGRS.2015.2462074

Peng, J., Niesel, J., & Loew, A. (2015). Evaluation of soil moisture downscaling using a simple thermal-based proxy – the REMEDHUS network (Spain) example. *Hydrol. Earth Syst. Sci.*, *19*, 4765–4782. https://doi.org/10.5194/hess-19-4765-2015

Pettorelli, N. (2013a). NDVI from A to Z. In N. Pettorelli (Ed.), *The Normalized Difference Vegetation Index* (p. 0). Oxford University Press. https://doi.org/10.1093/acprof:osobl/9780199693160.003.0003

Pettorelli, N. (2013b). Vegetation indices. In N. Pettorelli (Ed.), *The Normalized Difference Vegetation Index* (p. 0). Oxford University Press. https://doi.org/10.1093/acprof:osobl/9780199693160.003.0002

Profillidis, V. A., & Botzoris, G. N. (2019). Chapter 5—Statistical Methods for Transport Demand Modeling. In V. A. Profillidis & G. N. Botzoris (Eds.), *Modeling of Transport Demand* (pp. 163–224). Elsevier. https://doi.org/10.1016/B978-0-12-811513-8.00005-4

Ramachandran, K. M., & Tsokos, C. P. (2021). Chapter 6—Hypothesis testing. In K. M. Ramachandran & C. P. Tsokos (Eds.), *Mathematical Statistics with Applications in R (Third Edition)* (pp. 253–300). Academic Press. https://doi.org/10.1016/B978-0-12-817815-7.00006-3

Rostami, A., Raeini-Sarjaz, M., Chabokpour, J., & Chadee, A. A. (2023). *Soil moisture monitoring by downscaling of remote sensing products using LST/VI space derived from MODIS products*. *23*(2), 688–705. https://doi.org/10.2166/ws.2023.002

Rouse, J. W., Jr., Haas, R. H., Schell, J. A., & Deering, D. W. (1974). Monitoring Vegetation Systems in the Great Plains with Erts. *NASA Special Publication*, *351*, 309.

Seneviratne, S. I., Corti, T., Davin, E. L., Hirschi, M., Jaeger, E. B., Lehner, I., Orlowsky, B., & Teuling, A. J. (2010). Investigating soil moisture–climate interactions in a changing climate: A review. *Earth-Science Reviews*, *99*(3), 125–161. https://doi.org/10.1016/j.earscirev.2010.02.004

Tian, J., Deng, X., & Su, H. (2019). Intercomparison of two trapezoid-based soil moisture downscaling methods using three scaling factors. *International Journal of Digital Earth*, *12*(4), 485–499. https://doi.org/10.1080/17538947.2018.1447031

Tiruneh, G. A., Meshesha, D. T., Adgo, E., Tsunekawa, A., Haregeweyn, N., Fenta, A. A., & Reichert, J. M. (2022). Exploring crop yield variability under different land management practices with spectral vegetation indices in the Ethiopian Blue Nile basin. *Geocarto International*, *37*(27), 15896–15911. https://doi.org/10.1080/10106049.2022.2102239

USGS. (n.d.). *Landsat 5*. USGS. Retrieved 8 May 2023, from https://www.usgs.gov/landsat-missions/landsat-5

Wan, Z., Wang, P., & Li, X. (2004). Using MODIS Land Surface Temperature and Normalized Difference Vegetation Index products for monitoring drought in the southern Great Plains, USA. *International Journal of Remote Sensing*, *25*(1), 61–72. https://doi.org/10.1080/0143116031000115328

Xiang, G., Huete, A. R., Ni, W., & Miura, T. (2000). *Optical–Biophysical Relationships of Vegetation Spectra without Background Contamination*. *74*(3), 609–620. https://doi.org/10.1016/S0034-4257(00)00150-4

Xu, C., Qu, J. J., Hao, X., Cosh, M. H., Prueger, J. H., Zhu, Z., & Gutenberg, L. (2018). Downscaling of Surface Soil Moisture Retrieval by Combining MODIS/Landsat and In Situ Measurements. *Remote Sensing*, *10*(2), 210. https://doi.org/10.3390/rs10020210

Xu, X., & Frey, S. K. (2021a). Validation of SMOS, SMAP, and ESA CCI Soil Moisture Over a Humid Region. *IEEE Journal of Selected Topics in Applied Earth Observations and Remote Sensing*, *14*, 10784–10793. https://doi.org/10.1109/JSTARS.2021.3122068

Xu, X., & Frey, S. K. (2021b). Validation of SMOS, SMAP, and ESA CCI Soil Moisture Over a Humid Region. *IEEE Journal of Selected Topics in Applied Earth Observations and Remote Sensing*, *14*, 10784–10793. https://doi.org/10.1109/JSTARS.2021.3122068

Yang, Z., Shrestha, R., Crow, W., Bolten, J., Mladenova, I., Yu, G., & Di, L. (2016). Evaluation of Assimilated Smos Soil Moisture Data for Us Cropland Soil Moisture Monitoring. *2016 Ieee International Geoscience and Remote Sensing Symposium (Igarss)*, 5244–5247. https://doi.org/10.1109/IGARSS.2016.7730366

Zhang, Y., Chen, Y., Chen, L., Xu, S., & Sun, H. (2022). A machine learning-based approach for generating high-resolution soil moisture from SMAP products. *Geocarto International*, *37*(27), 16086–16107. https://doi.org/10.1080/10106049.2022.2105406

Zhao, W., Li, A., Jin, H., Zhang, Z., Bian, J., & Yin, G. (2017). *Performance Evaluation of the Triangle-Based Empirical Soil Moisture Relationship Models Based on Landsat-5 TM Data and In Situ Measurements*. *55*(5), 2632–2645. https://doi.org/10.1109/TGRS.2017.2649522

Zhao, W., Wen, P. F., & Cai, J. F. (2022). *Methods, progresses, and challenges of passive microwave soil moisture spatial downscaling*. *26*(9), 1699–1722. https://doi.org/10.11834/jrs.20210515

Zhu, Z., Bo, Y., & Sun, T. (2023). Spatial downscaling of satellite soil moisture products based on apparent thermal inertia: Considering the effect of vegetation condition. *Journal of Hydrology*, *616*, 128824. https://doi.org/10.1016/j.jhydrol.2022.128824

Appendix

Table A1. The used ISMN stations for the REMEDHUS and SMOSMANIA networks. The temporal range used and their landcover types.

REMEDHUS			SMOSMANIA		
ID	**Temporal range**	**Landcover**	**ID**	**Temporal range**	**Landcover**
F6	2010-2012	Agriculture	**BRN**	2018-2021	Broad-leaved forest
F11	2010-2012	Non-irrigated arable land	**BRZ**	2018-2021	Pastures
H7	2010-2012	Vineyards	**CBR**	2018-2021	Complex cultivation patterns
H9	2010-2012	Permanently irrigated land	**CDM**	2018-2021	Vineyard
H13	2010-2012	Non-irrigated arable land	**LGC**	2018-2021	Coniferous forest
I6	2010-2012	Non-irrigated arable land	**LHS**	2018-2021	Non-irrigated arable land
J3	2010-2012	Non-irrigated arable land	**LZG**	2018-2021	Airport
K4	2010-2012	Permanently irrigated land	**MJN**	2018-2021	Broad-leaved forest
K10	2010-2012	Non-irrigated arable land	**MNT**	2018-2021	Pasture
K13	2010-2012	Non-irrigated arable land	**MTN**	2018-2021	Pasture
L3	2010-2012	Non-irrigated arable land	**MZN**	2018-2021	Coniferous forest
L7	2010-2012	Non-irrigated arable land	**NBN**	2018-2021	Sclerophyllous vegetation
M5	2010-2012	Non-irrigated arable land	**PRD**	2018-2021	Vineyard
M9	2010-2012	Permanently irrigated land	**PRG**	2018-2021	Non-irrigated arable land
M13	2010-2012	Non-irrigated arable land	**PZN**	2018-2021	Vineyard
N9	2010-2012	Non-irrigated arable land	**SFL**	2018-2021	Complex cultivation patterns
O7	2010-2012	Non-irrigated arable land	**SVN**	2018-2021	Non-irrigated arable land
Data obtained from https://ismn.earth/en/dataviewer/			**VLV**	2018-2021	Vineyard